SCIENCE CHINA PRESS

SCIENCE CHINA Chemistry 2026 69(9): 5204–5220
https://doi.org/10.1007/s11426-025-3433-0

ARTICLES

# Mitochondrial nanomotors prevent the progression of liver fibrosis

Lin Chen, Xingyu Lin, Keheng Wang, Yu Duan, Zhuolin Wu, Ziyu Wu, Min Zhou, Chun Mao* & Mimi Wan*

Department of Vascular Surgery, Cardiovascular Medical Center, Nanjing Drum Tower Hospital, National and Local Joint Engineering Research Center of Biomedical Functional Materials, School of Chemistry and Materials Science, Nanjing Normal University, Nanjing 210023, China
*Corresponding authors (email: maochun@njnu.edu.cn; wanmimi@njnu.edu.cn)

Received 13 October 2025; Accepted 22 March 2026; Published online 17 August 2026

**Abstract** Mitochondrial transplantation holds promise in halting the advancement of liver fibrosis. However, the presence of capillarized liver sinusoids and an excessive accumulation of extracellular matrix (ECM) pose significant challenges to unmodified mitochondria. To surmount these obstacles, we introduce a novel approach that employs sulfur dioxide ($SO_2$)-releasing nanomotors to facilitate rapid mitochondrial transplantation. The strategy utilizes an L-cysteine-based monomer that is polymerized *in situ* on the surface of mitochondria, creating a protective polymer layer to form mitochondrial nanomotors. The inclusion of L-cysteine enables the mitochondria to chemotactically navigate towards areas of liver damage, where levels of cysteine dioxygenase and aspartate aminotransferase are elevated, and to penetrate deeply into the damaged tissue. The $SO_2$ generated during this process can revert the fenestrated phenotype of liver sinusoidal endothelial cells within an hour by activating intrinsic pathways, thereby effectively reducing the ECM and aiding in the repair of damaged hepatocytes. To account for the variability in fibrosis progression, we have developed mouse models with both mild and severe liver fibrosis. Specifically, the transcriptome results of the mouse liver tissue after treatment confirm that this method can effectively improve mitochondrial-related functions, thereby providing a good therapeutic effect at the genetic level.

**Keywords** mitochondrial transplantation, nanomotors, sulfur dioxide, liver fibrosis

## 1 Introduction

Liver fibrosis is an inescapable pathological process and a defining characteristic in the escalation from chronic liver injury to severe downstream complications, including cirrhosis and hepatocellular carcinoma, and more than 2 million people die from liver-related diseases every year [1,2]. Research indicates that liver fibrosis is a dynamic and reversible condition, making the prevention of its progression crucial for managing liver diseases [3]. Liver fibrosis is an excessive wound healing reaction of the liver [4]. Damage to hepatocyte mitochondria, induced by external factors such as alcohol, metabolic issues, drugs, and chemical toxins, releases danger signal molecules and reactive oxygen species (ROS), triggering inflammation and activating hepatic stellate cells (HSCs) [3,5–7]. When impaired mitochondria fail to neutralize the excess ROS, oxidative stress ensues, exacerbating hepatocyte damage and leading to cell death [8,9]. Concurrently, this process is marked by the capillarization of sinusoids, diminished permeability in liver sinusoidal endothelial cells (LSECs) and an overabundance of extracellular matrix (ECM) deposition, primarily collagen types I and III. These factors impede the infiltration of essential nutrients, such as plasma proteins, into the liver tissue [10,11].

Unfortunately, despite the critical need for effective treatments for liver fibrosis, the anti-fibrosis medications in clinical use are primarily repurposed drugs, aiming to mitigate the progression of liver fibrosis through anti-inflammatory, hepatoprotective, and antioxidant actions [12,13]. These drugs offer some respite from the existing deterioration but are incapable of halting the ongoing hepatocyte damage [14]. Meanwhile, researchers have developed nanomaterial-based drug delivery systems, which have the potential to significantly enhance drug efficacy [15,16]. Yet, the success of these strategies is still predicated on the mechanisms of the drugs themselves, with most only providing symptomatic relief and failing to prevent the advancement of liver fibrosis. In principle, an effective treatment for liver fibrosis must address both the existing deterioration, including capillarized liver sinusoids and excessive ECM deposition, and the root causes of hepatocyte damage to facilitate the effective repair of impaired hepatocytes [17,18]. As reported in the literature, the initial event leading to liver fibrosis is mitochondrial dysfunction of hepatocytes [19–21]; thus, transplanting functional mitochondria into fibrotic liver to replace dysfunctional mitochondria seems to be a crucial strategy for restoring hepatocyte function [22–24]. However, the practical effectiveness of this strategy is still limited by the challenges that unmodified mitochondria face in navigating the existing deterioration, particularly in penetrating the barriers posed by capillarized sinusoids and excessive ECM. Meantime, the inflammatory microenvironment may destroy the activity of mitochondria [25]. Therefore, while mitochondrial transplantation holds promise for treating liver fibrosis, the strategy is still in its infancy due to the complexities of the pathological microenvironment specific to liver fibrosis.

Here, sulfur dioxide ($SO_2$)-releasing nanomotors were constructed on the mitochondrial surface to protect the activity of mitochondria and give mitochondria new functions, thereby facilitating efficient mitochondrial transplantation for liver fibrosis treatment (Figure 1). Specifically, the L-cysteine-based zwitterionic monomer was reacted with the degradable crosslinker (responsible for ROS) to form a polymer layer on the mitochondrial surface through a free radical polymerization reaction to construct mitochondrial nanomotors.

**Citation:** Chen L, Lin X, Wang K, Duan Y, Wu Z, Wu Z, Zhou M, Mao C, Wan M. Mitochondrial nanomotors prevent the progression of liver fibrosis. *Sci China Chem*, 2026, 69: 5204–5220. https://doi.org/10.1007/s11426-025-3433-0

© Science China Press 2026

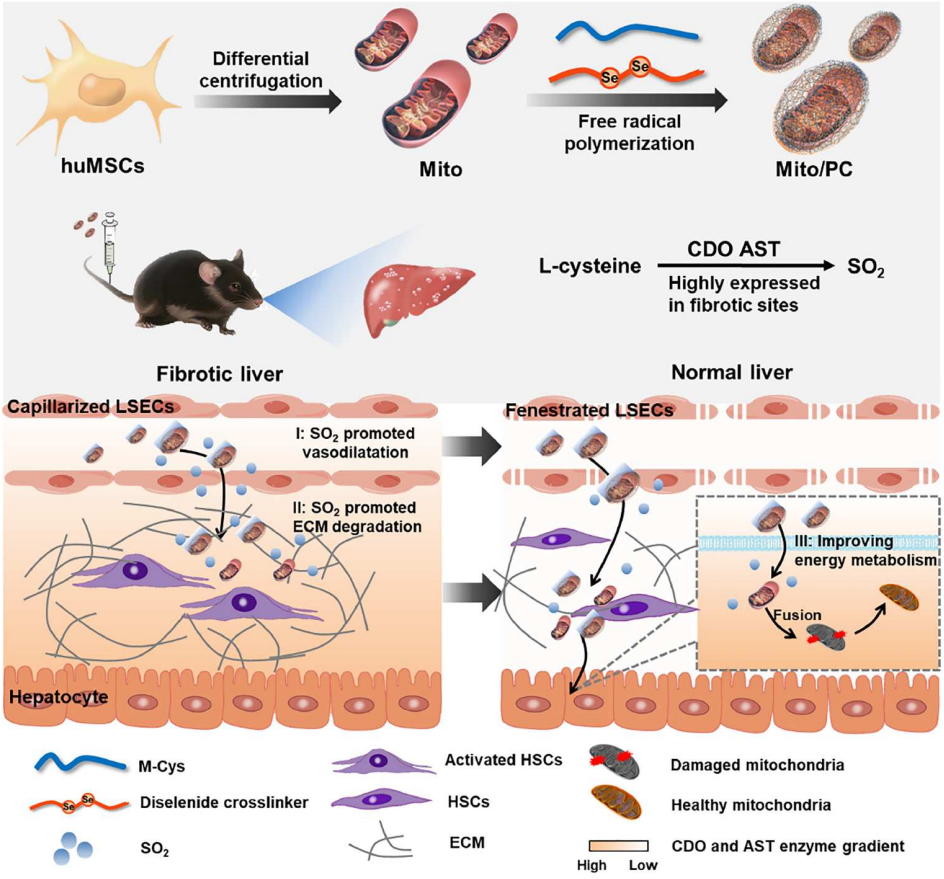



**Figure 1** (Color online) Schematic illustrating the fabrication of $SO_2$-releasing mitochondrial nanomotors Mito/PC and the treatment of liver fibrosis.

The L-cysteine structure can specifically bind to high concentrations of cysteine dioxygenase (CDO) and aspartate aminotransferase (AST), which are released from damaged hepatocytes during liver injury, establishing a concentration gradient between the damaged hepatocytes and the liver sinusoids [26–30]. This gradient generates a chemotactic force that guides the mitochondrial nanomotors to the site of damage effectively. $SO_2$ released in this process can activate the soluble guanylyl cyclase/cyclic guanosine phosphate (sGC/cGMP) signaling pathway to restore the fenestrated phenotype and permeability of LSECs [31,32], which promotes the mitochondrial nanomotors to break through the capillarized sinusoids barrier and accumulate in the Disse space. Almost simultaneously, $SO_2$ released by mitochondrial nanomotors during this process can stimulate the production of nitric oxide (NO) [33,34], which can react with ROS to form peroxynitrite to stimulate the production of the active matrix metalloproteinase MMP-1, thereby degrading the collagen components in the ECM [35], thus promoting mitochondria to deeply penetrate the Disse space to restore energy metabolism and repair the damaged hepatocyte. The $SO_2$-releasing mitochondrial nanomotors can not only effectively alleviate the existing worsening outcome, such as capillarized liver sinusoids and ECM accumulation, but also treat the root cause by repairing damaged hepatocytes, thus preventing the progression of liver fibrosis.

## 2 Results and discussion

### 2.1 Physicochemical properties and bioactivity characterization of mitochondrial nanomotors

Human umbilical cord mesenchymal stem cells (huMSCs) were selected as the source of healthy mitochondria (Mito) [36]. To initially verify the successful isolation of mitochondria from huMSCs [37], intracellular mitochondria were labeled with MitoTracker Red probe prior to isolation, which displayed stable and significant intracellular red fluorescence around the nucleus (Figure 2a). The cells were immediately lysed and mitochondria were isolated according to the standard protocol. The resulting suspension showed similar red fluorescence representing Mito (Figure 2b). Transmission electron microscope (TEM) image showed that the morphology of Mito was sphere-like (Figure 2c), dynamic light scattering (DLS) showed that the hydrodynamic diameter of Mito was about 500 nm (Figure 2e), and the Zeta potential was about −13.1 mV (Figure 2f). After that, mitochondrial nanomotors were constructed. Firstly, L-cysteine was reacted with methacryloyl chloride to obtain *N*-methylacrylyl-*L*-cysteine monomer (M-Cys) (Figure S1, Supporting Information online), which was characterized by $^1$H nuclear magnetic resonance (NMR) (Figure S2) [38]. Meanwhile, a diselenide crosslinker responsive to ROS degradation was synthesized and characterized (Figures S3 and S4) [39,40]. In the ammonium persulfate/tetramethylenediamine (APS/TEMED) system [36], by using M-Cys and a diselenide crosslinker to construct a polymer layer *in situ* on the surface of Mito through a free radical polymerization reaction, mitochondrial nanomotors named Mito/PC were obtained (Figure S5). Compared to Mito, the TEM image showed that Mito/PC had a rough surface with a distinct coating (Figure 2d). Besides, an increase in hydrodynamic diameter of about 200 nm (Figure 2e) and a more negative surface charge were also observed (Figure 2f). Using Cy5-labeled M-Cys (green fluorescence) and MitoTracker Red CMXRos-labeled Mito (red fluorescence) to perform the above modification process, it was observed that there was good fluorescence co-localization in Mito/PC

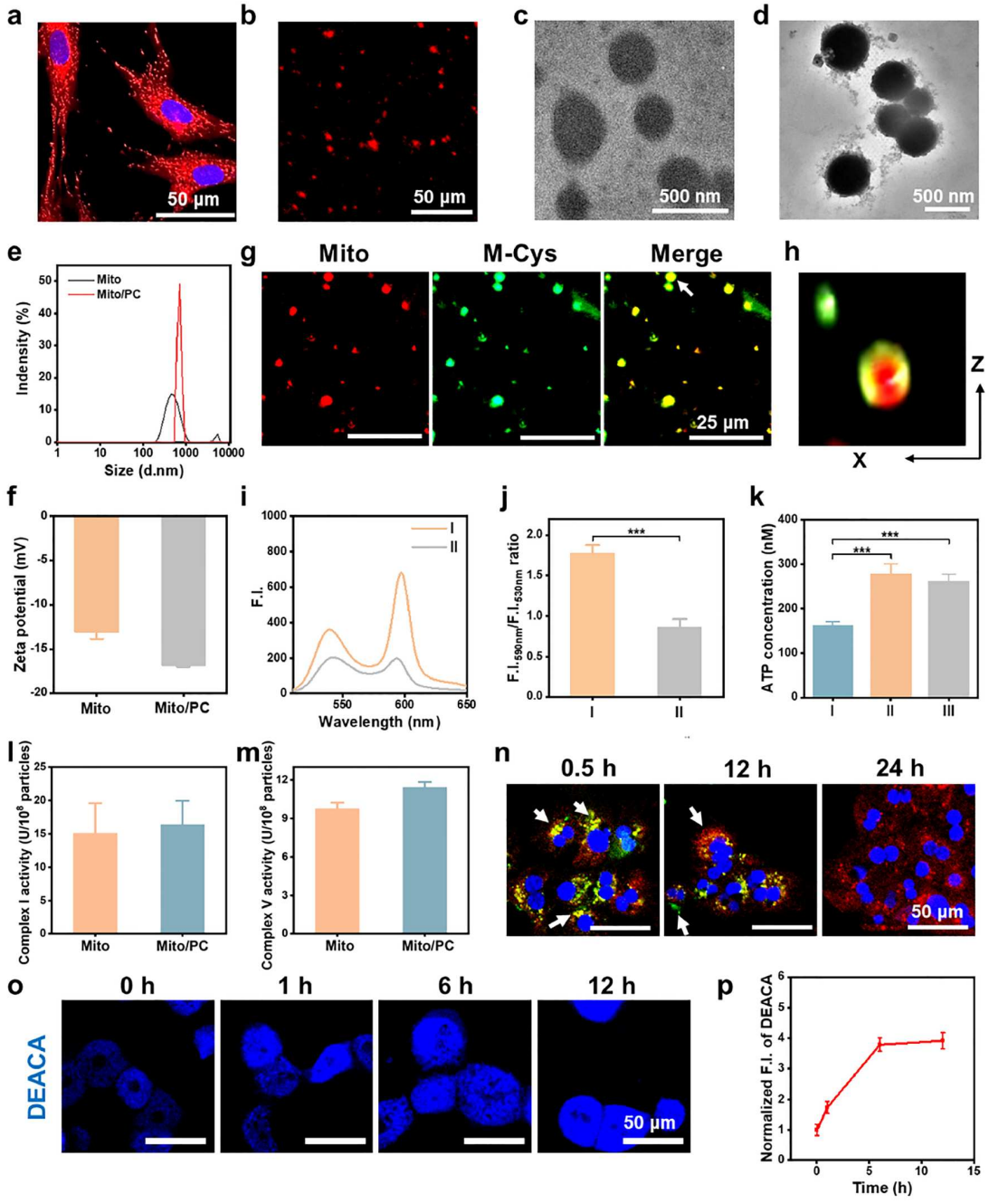



**Figure 2** (Color online) Physicochemical properties and biological activities of mitochondrial nanomotors. Fluorescence images of MitoTracker Red-labeled (a) huMSCs (before isolation) (blue, nucleus stained with Hoechst 33342) and (b) Mito (after isolation). TEM images of (c) Mito and (d) Mito/PC. (e) Hydrodynamic diameter and (f) Zeta potential of Mito and Mito/PC ($n$=3). (g) Fluorescence co-location images of Mito/PC (red, Mito stained with Mito-Tracker Red CMXRos; green, M-Cys stained with Cy5). (h) CLSM image of 3D tomography of the particle pointed by the arrow in g. (i) Fluorescence spectra and (j) corresponding $F.I._{590nm}/F.I._{530nm}$ ratio of different samples stained with JC-1 (I, Mito/PC; II, Mito/PC treated with antimycin A) ($n$=3). (k) Ability of different samples to synthesize ATP in the case of providing substrate glutamic acid, malic acid and ADP (I, Mito treated with antimycin A; II, Mito; III, Mito/PC) ($n$=3). Activity of mitochondrial respiratory chain (l) complex I and (m) complex V of different samples ($n$=3). (n) Fluorescence co-localization images of MitoTracker Red CMXRos-labeled Mito and Cy5-labeled M-Cys in Mito/PC incubated in pre-stimulated primary hepatocytes for different times. (o) Fluorescence images of released $SO_2$ in pre-stimulated primary hepatocytes treated with Mito/PC for different times (blue, $SO_2$ stained with DEACA). (p) Quantitative analysis of average DEACA fluorescence intensity per cell in o ($n$=3). Experimental data are means ± SD of samples in a representative experiment. *$P$ < 0.05, **$P$ < 0.01, and ***$P$ < 0.001, determined by one-way ANOVA or independent-samples $T$ test.

(Figure 2g), and the red fluorescence could only be exposed when the green fluorescence was gradually stripped away (Figure 2h and Movie S1, Supporting Information online). However, after the direct mixture of M-Cys and Mito without polymerization, most of the red fluorescence of mitochondria existed alone (Figure S6). These results indicated that the nanomotor coating was on the mitochondrial surface. In addition, flow cytometry results showed that the efficiency of this modification process was highly efficient and could reach up to 99.1% (Figure S7).

Further, we assessed whether the modification process would affect mitochondrial biological function using multiple indicators. SDS-PAGE Coomassie blue staining showed that Mito/PC maintained a similar protein expression profile to Mito (Figure S8), indicating that the modification process hardly changed the surface proteins of mitochondria. Mitochondrial membrane potential is also an important indicator of mitochondrial biological activity. JC-1 dye, a cationic carbocyanine dye, is commonly used to detect mitochondrial membrane integrity by detecting mitochondrial

membrane potential [41]. When the mitochondrial membrane potential is normal, JC-1 forms aggregates emitting red fluorescence (590 nm) due to the increased concentration in mitochondria. When mitochondrial membrane potential collapses (such as when mitochondrial respiration is inhibited by antimycin A), JC-1 is released from mitochondria, reduced in concentration, and reversed into monomer form emitting green fluorescence (530 nm) [42]. The above process can be used to characterize whether the mitochondrial membrane potential remains stable during the modification process.

When normal Mito was incubated with JC-1, the fluorescence spectrum of JC-1 showed an obvious absorption peak at 590 nm, indicating that the mitochondrial membrane potential was relatively complete ($F.I._{590nm}/F.I._{530nm}$ ratio was about 2.4). After being treated with antimycin A, the peak intensity at 590 nm was greatly reduced, and the $F.I._{590nm}/F.I._{530nm}$ ratio was reduced to 0.7 (Figure S9), indicating the collapse of mitochondrial membrane potential. For Mito/PC, JC-1 also existed in the form of aggregates, and the red fluorescence at 590 nm was strong ($F.I._{590nm}/F.I._{530nm}$ ratio was about 1.8). After treatment with antimycin A, the red fluorescence at 590 nm was greatly weakened ($F.I._{590nm}/F.I._{530nm}$ ratio was reduced to 0.9) (Figure 2i, j). This result was consistent with the fluorescence imaging. After treatment with antimycin A, the red fluorescence of Mito/PC stained with JC-1 significantly decreased to 13.4% of the normal level, while the green fluorescence significantly increased (Figure S10). The above results showed that the modification process had little effect on the mitochondrial membrane potential, and Mito/PC retained relatively complete membrane potential. Further, the ability of mitochondrial nanomotors to produce adenosine triphosphate (ATP) was also tested. In the case of providing substrate glutamic acid, malic acid and adenosine-diphosphate (ADP) [43], compared with Mito treated with antimycin A (the ability to produce ATP was destroyed), Mito/PC can effectively produce ATP, which was comparable to that of Mito (Figure 2k). Meanwhile, compared with Mito, Mito/PC had similar levels of mitochondrial respiratory chain complex I and complex V (Figure 2l, m), and did not produce excessive ROS (Figure S11). All the above results demonstrated that the modification process retained the original biological functions of mitochondria.

Since the diselenide crosslinker in the nanomotor structure can gradually degrade into polymer chain segments with lower molecular weight in response to ROS [39,40], we explored the degradation of the nanomotor coating on the mitochondrial surface in the pre-stimulated primary hepatocytes. It was observed that, as the incubation time increased, the green fluorescence representing the nanomotor coating gradually separated from the red fluorescence representing the mitochondria (from 0.5 to 12 h) until it almost disappeared (24 h) (Figure 2n and Figure S12). Subsequently, the ability of mitochondrial nanomotors to release $SO_2$ in hepatocytes was tested, and the 7-diethylaminocoumarin-3-aldehyde (DEACA) probe was used to label $SO_2$ [44]. Hepatocyte L-02 cells incubated with Mito/PC showed clear blue fluorescence (representing $SO_2$), and the fluorescence intensity was 5.8 times that of the control group, while cells incubated with Mito showed only a small amount of blue fluorescence (Figure S13). Additionally, after Mito/PC was incubated in the pre-stimulated primary hepatocytes for 6 h, the amount of $SO_2$ released by nanomotors reached equilibrium (Figure 2o, p and Figure S14), indicating that there should be no risk of prolonged exposure to $SO_2$. In particular, the $SO_2$ release behavior of mitochondrial nanomotors in different cells was examined. Compared with the respective control group (cells without Mito/PC), there was no significant difference in blue fluorescence in Raw 264.7 cells and HUVECs treated with Mito/PC ($F.I._{Mito/PC}/F.I._{Ctrl}$ ratio was 1.0 and 0.9, respectively). Blue fluorescence in LX-2 cells was slightly increased ($F.I._{Mito/PC}/F.I._{Ctrl}$ ratio was 1.7), but its intensity was much lower than that in primary hepatocytes ($F.I._{Mito/PC}/F.I._{Ctrl}$ ratio was 4.8) (Figure S15). These results indicated that the mitochondrial nanomotors (containing the substrate L-cysteine) can specifically release $SO_2$ in hepatocytes with high concentrations of CDO and AST.

## 2.2 Characterization of motion and chemotactic behavior of mitochondrial nanomotors

The reason why nanomotors can produce motion behavior is that there are asymmetric forces [45]. The asymmetric force of mitochondrial nanomotors constructed in this work comes from the enzyme-substrate-specific interaction between the substrate in nanomotors and the enzymes highly expressed in the fibrotic liver. Specifically, the fibrotic liver is characterized by elevated levels of CDO and AST, which leak from damaged hepatocytes, establishing a concentration gradient between the affected liver area and the liver sinusoids [26–30]. The presence of L-cysteine in the mitochondrial nanomotors allows them to sensitively detect this gradient of CDO and AST and engage in enzyme-substrate-specific interactions. During this interaction, the L-cysteine substrate is catalyzed by CDO and AST [31], leading to the production of $SO_2$, which in turn guides the nanomotors chemotactically to the fibrotic site.

The motion behavior of mitochondrial nanomotors was first evaluated in different cellular environments, including L-02 cells with high concentrations of CDO and AST, and HUVECs without high concentrations of CDO and AST, respectively. In the lysate of L-02 cells, compared to the Brownian motion of Mito (the mean speed was only 1.2 μm $s^{-1}$) (Figure 3a and Movie S2), Mito/PC showed significant displacement and different direction of motion, and the mean speed reached about 3.4 μm $s^{-1}$ (Figure 3c and Movie S4). In contrast, in the lysate of HUVECs, both Mito and Mito/PC exhibited obvious Brownian motion trajectories with speed distributions less than 1.5 μm $s^{-1}$ (Figure 3b, d and Movies S3 and S5). In addition, we evaluated the motion behavior of particles by calculating their equivalent diffusion coefficient $D_{eff}$ through the mean square displacement (MSD) curve [46,47]. As shown in Figure S16, the $\Delta L^2$-$\Delta t$ for Mito in the lysate of L-02 and HUVECs environments conformed to a linear fit, with $R^2 \geqslant 0.9$, and $D_{eff}$ of 0.3 and 0.4 $\mu m^2\ s^{-1}$, respectively, indicating diffusive motion. Consistent with this result, the $\Delta L^2$-$\Delta t$ for Mito/PC in different cell lysate environments also conformed to a linear fit, with $R^2 \geqslant 0.9$. Specifically, the $D_{eff}$ for Mito/PC in the lysate of HUVECs environment was 0.5 $\mu m^2\ s^{-1}$, indicating diffusive motion, while the $D_{eff}$ for Mito/PC in the lysate of L-02 cells environment increased to 1.3 $\mu m^2\ s^{-1}$, suggesting that Mito/PC exhibited enhanced diffusion in high concentrations of CDO and AST environments.

Further, a static Y-shaped channel model was used to evaluate the chemotactic behavior of mitochondrial nanomotors in the cellular environment with high concentrations of CDO and AST [48]. Agarose gels containing lysate of L-02 cells (with chemical attractants, high concentrations of CDO and AST) and HUVECs (without chemical attractants) were added to the corresponding reservoirs II and III, respectively, causing the CDO and AST to diffuse in the channels and create a concentration gradient. MitoTracker Red-labeled Mito/PC was added to reservoir I, and the fluorescence intensity changes in reservoir II and reservoir III at different time points were observed by inverted fluorescence microscopy (Figure 3e). Over time, the fluorescence intensity of Mito/PC increased significantly in reservoir II, but only slightly changed in reservoir III. Moreover, the fluorescence intensity of Mito/PC in reservoir II was significantly stronger than that in

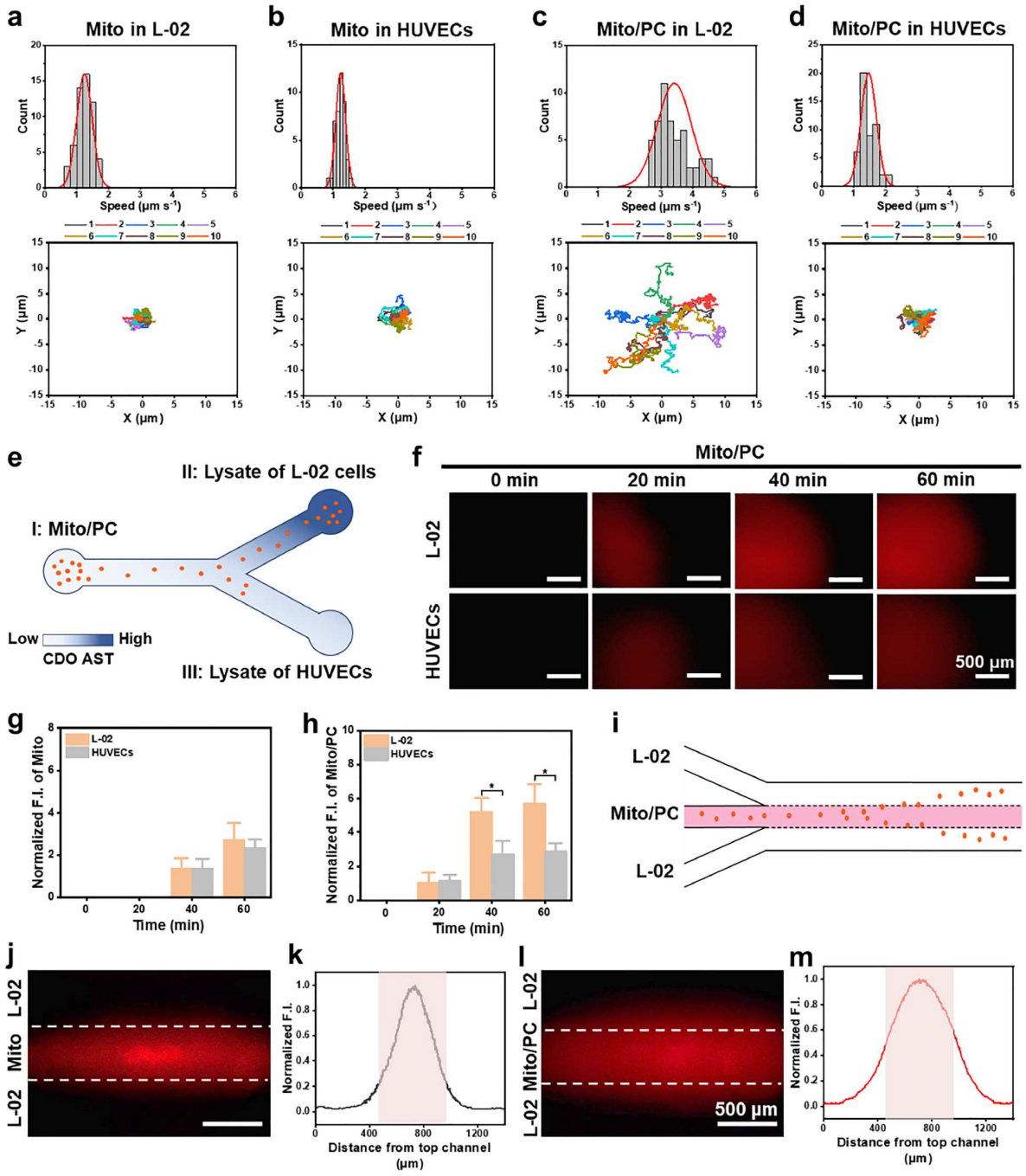



**Figure 3** (Color online) Evaluation of motion and chemotactic behavior of mitochondrial nanomotors. The distribution of speed ($n$=50) and the trajectory ($n$=10) of (a) Mito in the lysate of L-02 cells environment, (b) Mito in the lysate of HUVECs environment, (c) Mito/PC in the lysate of L-02 cells environment and (d) Mito/PC in the lysate of HUVECs environment. (e) Schematic illustration of a Y-shaped channel: reservoir I was MitoTracker Red-labeled Mito/PC, reservoir II was agarose gel containing lysate of L-02 cells, and reservoir III was agarose gel containing lysate of HUVECs. (f) Fluorescence images of Mito/PC in reservoir II and III of the Y-shaped channel at different time points. Corresponding normalized fluorescence quantitative results of (g) Mito and (h) Mito/PC in reservoir II and III of the Y-shaped channel ($n$=3). (i) Schematic illustration of Ψ-shaped microfluidic channel. Channels I and III were the flow of the lysate of L-02 cells; Channel II was the flow of MitoTracker Red-labeled Mito/PC. (j) Representative fluorescence image and (k) corresponding normalized fluorescence distribution of Mito flow. (l) Representative fluorescence image and (m) corresponding normalized fluorescence distribution of Mito/PC flow. Experimental data are means ± SD of samples in a representative experiment. *$P$ < 0.05, **$P$ < 0.01, and ***$P$ < 0.001, determined by independent-samples $T$ test.

reservoir III at 60 min, which was 1.9 times that of reservoir III, indicating that Mito/PC could sensitize the concentration gradient of CDO and AST and exhibit chemotactic behavior (Figure 3f, h). In contrast, there was little difference in the fluorescence intensity of Mito in reservoir II and reservoir III at different time points (Figure 3g and Figure S17). Calculation results indicated that the concentrations of CDO and AST used in the agarose gel block in reservoir II of the Y-channel were much lower than those in the liver tissue of $CCl_4$ modeling (Figure S18). Despite the lower concentration gradient, the mitochondrial nanomotors still exhibited chemotactic behavior, suggesting that mitochondrial nanomotors should demonstrate even more pronounced chemotactic behavior towards *in vivo* liver tissue with higher CDO and AST concentration gradients.

In addition, the chemotactic behavior of mitochondrial nanomotors in a fluid environment was characterized by the dynamic Ψ-shaped microfluidic chip (Figure 3i) [48]. When the fluid on both sides of the chip was the lysate of L-02 cells, and the fluid in the

middle channel was MitoTracker Red-labeled Mito/PC, the chemotactic behavior of Mito/PC was determined by observing the change in fluorescence intensity perpendicular to the flow direction near the exit of the fluid with an inverted fluorescence microscope. It can be observed that the red fluorescence moved to both sides, and the fluorescence intensity was strongest in the middle position, while the fluorescence intensity on both sides gradually decreased. The fluorescence signal can be diffused from the middle channel to the channels with lysate of L-02 cells on both sides (Figure 3l, m), which was a result of chemotaxis of Mito/PC to the environment containing high concentrations of CDO and AST. When the fluid on both sides was the lysate of L-02 cells and the middle channel fluid was MitoTracker Red-labeled Mito, the fluorescence signal was concentrated in the middle channel, and there was almost no fluorescence signal on both sides (Figure 3j, k). In addition, when the bilateral channel fluid was the lysate of HUVECs, neither Mito nor Mito/PC showed significant bilateral chemotactic behavior (Figure S19).

## 2.3 Mechanism of mitochondrial nanomotors restoring the fenestrated phenotype of primary LSECs *in vitro*

In fibrotic liver, LSECs lose the normal differentiated phenotype, and the permeability decreases, thus obstructing the transport of therapeutic agents through the sinusoids to the Disse space. Studies have shown that the fenestrated phenotype of LSECs is influenced by the sGC/cGMP pathway [32], which can be regulated by the gas signaling molecule $SO_2$ [31,49]. As shown in the mechanism diagram in Figure 4a, $SO_2$ released by mitochondrial nanomotors can upregulate the expression of cGMP and reduce the level of $Ca^{2+}$, thus playing a role in vasodilation and restoring the fenestrated phenotype of LSECs. Therefore, normal mouse primary LSECs were used to test this process.

Initially, we conducted a preliminary verification to confirm the successful isolation of primary LSECs from normal mouse liver. It is known from previous research that CD14, which is not typically found on regular vascular endothelial cells, is specifically expressed on LSECs in healthy livers [50]. The immunofluorescence staining results for CD14 revealed that the primary LSECs were CD14-positive, whereas the immortalized HUVECs were CD14-negative, as depicted in Figure S20. Subsequently, we verified the existence of fenestrae in LSECs. SEM images showed that primary LSECs cultured for 6 h showed many fenestrae (porosity was about 16.5%), but the quantity of the fenestrae gradually decreased with the increase of culture time, indicating the gradual loss of differentiated phenotype [17,51]. However, HUVECs always showed a capillarized phenotype (Figure S21). These results demonstrated the successful isolation of primary LSECs from normal mice, and the expression of CD14 and fenestrated phenotype was different from that of ordinary vascular endothelial cells.

We then investigated the uptake of mitochondrial nanomotors by LSECs. Different samples labeled with MitoTracker Red probe were co-incubated with LSECs for 24 h while the lysate of hepatocytes was added to simulate the fibrotic liver microenvironment (containing high concentrations of CDO and AST). Confocal laser scanning microscope (CLSM) images showed a 2.1-fold increase in fluorescence intensity of Mito/PC uptake by LSECs compared to Mito (Figure 4b, c and Figure S22), demonstrating that the motional behavior of mitochondrial nanomotors made it easier to be captured by cells [52]. Next, the ability of Mito/PC to restore the fenestrated phenotype of LSECs was examined. Following the culture period of 24 h that induced a capillarized phenotype in LSECs, we introduced different samples and incubated for an additional 24 h, including the addition of hepatocyte lysate. SEM images showed that LSECs treated with Mito/PC had a markedly increased number of fenestrae, with a porosity of about 13.9%, and exhibited a return to a more differentiated state compared to untreated cells and those in the Mito group, which had porosities of approximately 0.3% and 0.2%, respectively (Figure 4d, e). In addition, compared with LSECs cultured for 24 h (that is, Mito/PC treated for 0 h), the quantity of the fenestrae gradually increased with the increase of Mito/PC incubation time. The porosity was significantly restored at 1 h (about 9.4%), and basically returned to the normal level at 3 h (about 11.6%) (Figure 4f, g). These results indicated that mitochondrial nanomotors can rapidly reverse the capillarized state of LSECs. Consistent with this trend, immunofluorescent staining of CD31 (a classic marker of capillarized LSECs) showed that, compared with untreated LSECs, the expression of CD31 in LSECs treated with Mito/PC decreased to 60.1%, while there was no significant change in the Mito group (Figure 4h, i and Figure S23). In addition, we verified the pathway mechanism of $SO_2$-releasing nanomotors to restore the fenestrated phenotype of LSECs. Compared to the untreated group and the ODQ ( an sGC inhibitor) treated group [53], cGMP levels in LSECs treated with Mito/PC increased to 1.5 times (Figure 4j), and $Ca^{2+}$ green fluorescence signal intensity decreased to 62.5% (Figure 4k, l and Figure S24). The above results indicated that $SO_2$ can restore the differentiation of LSECs via the sGC/cGMP pathway, which could occur within 1 h of the arrival of the mitochondrial nanomotors, thereby rapidly entering the liver tissue through blood vessels.

## 2.4 Assessment of the ability of mitochondrial nanomotors to penetrate the ECM barrier *in vitro*

The nanomotors' motion characteristics are highly advantageous for their efficient cellular internalization. Having established the specific $SO_2$ release and the locomotion of mitochondrial nanomotors within the L-02 cell environment, we then set out to assess how these motion properties influence the nanomotors' ability to penetrate the ECM barrier *in vitro*. In a Transwell model [54], type I collagen and LX-2 cells were pre-layered in the upper chamber, and L-02 cells were cultured in the lower chamber. Different samples labeled with MitoTracker Red probe and lysate of hepatocytes were added to the upper chamber, and CLSM was used to observe the red fluorescence intensity in the lower chamber (Figure 4m). Fluorescence images showed that there was only a small amount of red fluorescence signal in the lower chamber cells of the Mito group. In comparison, the Mito/PC group with motion ability had more obvious red fluorescence intensity and more cell uptake (Figure 4n and Figure S25). The normalized fluorescence quantitative results showed that the fluorescence intensity of the Mito/PC group was 22.8 times that of the Mito group (Figure 4o). These findings suggested that the locomotion of mitochondrial nanomotors significantly boosted their ability to penetrate the collagen barrier, a capability that was anticipated to facilitate deeper infiltration into the Disse space and, subsequently, enhance the uptake of transplanted mitochondria by compromised hepatocytes. This enhancement was expected to translate into improved therapeutic outcomes.

## 2.5 Ability of mitochondrial nanomotors to restore energy metabolism of damaged hepatocytes *in vitro*

The ultimate purpose of mitochondrial surface modification is to transport more mitochondria to the damaged hepatocyte after effectively breaking through the dual pathological barriers, and restore the energy metabolism to repair the damaged hepatocyte. Prior to further cell experiments, the cytotoxicity of mitochondrial

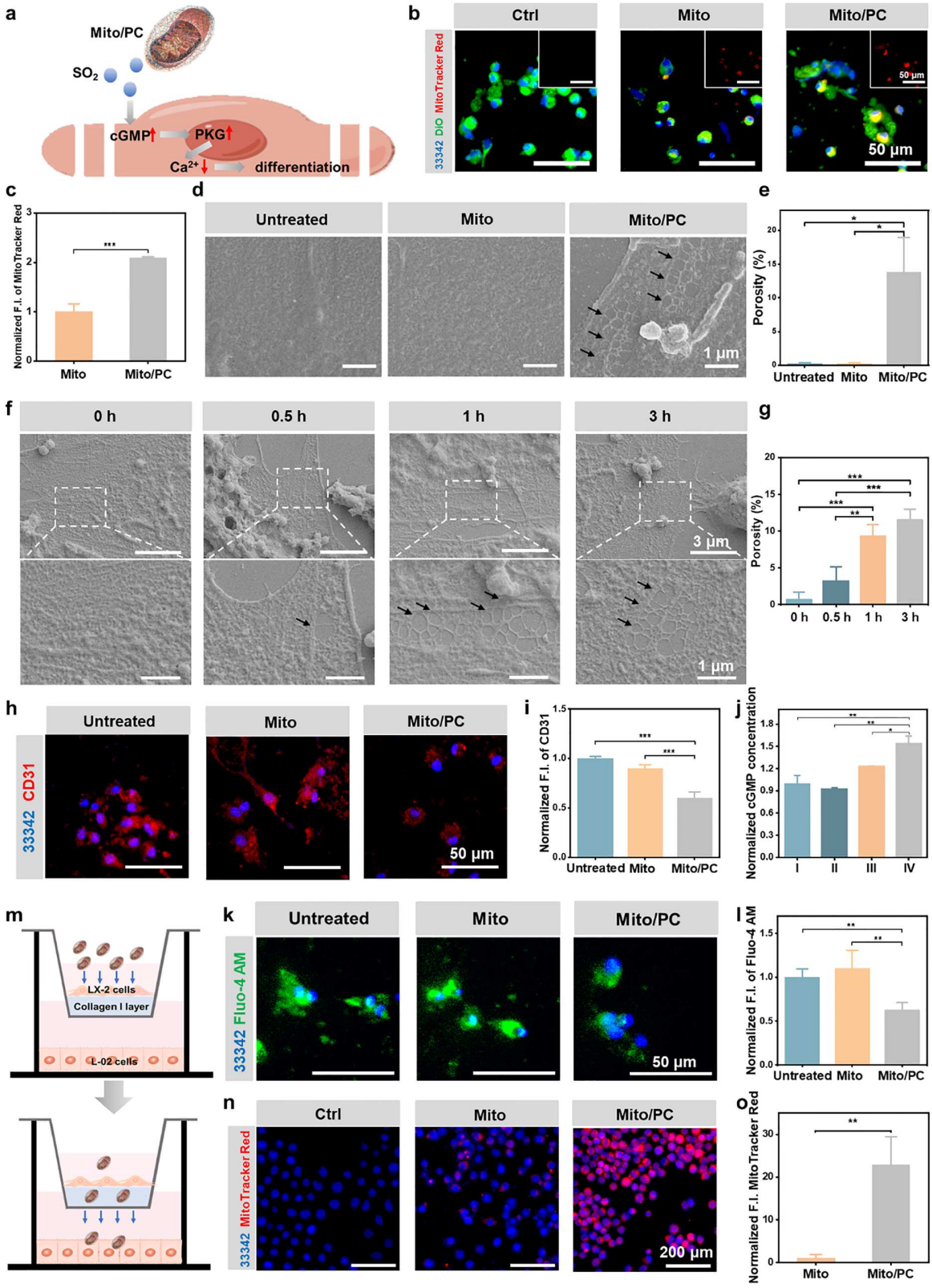



**Figure 4** (Color online) The ability of $SO_2$-releasing mitochondrial nanomotors to restore the fenestrated phenotype of LSECs and break through the ECM barrier *in vitro*. (a) Schematic illustration of the effect of mitochondrial nanomotors on the sGC/cGMP pathway in LSECs. (b) Fluorescence images of LSECs cellular uptake of different samples for 24 h (blue, nucleus stained with Hoechst 33342; red, MitoTracker Red-labeled samples; green, cell membrane stained with DiO). (c) Quantitative analysis of average MitoTracker Red fluorescence intensity in b ($n$=3). (d) SEM images of LSECs co-cultured with different samples for 24 h. (e) Quantification of LSECs porosity from SEM images as shown in d ($n$=4). (f) SEM images of LSECs co-cultured with Mito/PC for different times. (g) Quantification of LSECs porosity from SEM images as shown in f ($n$=3). (h) Fluorescence images and (i) quantitative analysis of CD31 in LSECs treated with different samples (blue, nucleus stained with Hoechst 33342; red, CD31) ($n$=3). (j) Normalized cGMP levels in LSECs co-cultured with different samples for 24 h (I, untreated; II, ODQ; III, Mito; IV, Mito/PC) ($n$=4). (k) Fluorescence images of $Ca^{2+}$ levels in LSECs with different samples for 24 h (blue, nucleus stained with Hoechst 33342; green, $Ca^{2+}$ stained with Fluo-4 AM). (l) Quantitative analysis of average Fluo-4 AM fluorescence intensity in k ($n$=4). (m) Schematic diagram of the Transwell model of collagen barrier. (n) Fluorescence images of L-02 cells (bottom) with different samples (blue, nucleus stained with Hoechst 33342; red, samples stained with MitoTracker Red). (o) Quantitative analysis of average MitoTracker Red fluorescence intensity in n ($n$=4). Experimental data are means ± SD of samples in a representative experiment. *$P$ < 0.05, **$P$ < 0.01, and ***$P$ < 0.001, determined by one-way ANOVA or independent-samples $T$ test.

nanomotors Mito/PC was evaluated, which showed good cytocompatibility against hepatocytes at the concentration of $2\times10^6$ mL$^{-1}$ and for 72 h (Figure S26). The uptake of mitochondrial nanomotors by hepatocytes and the associated uptake pathways were then evaluated in detail. The fluorescence intensity in L-02 cells after co-incubation with Mito/PC increased to 1.8 times compared with that in the Mito group (Figure S27), indicating that the motion behavior of nanomotors made it easier to be captured by L-02 cells. Consistent with this trend, real-time quantitative PCR results showed that, compared to the control group and the pre-stimulated damage group (expression levels of 1.1 and 0.8, respectively), the relative expression level of the Mito group increased to 1542, and the relative expression level of the Mito/PC group significantly increased to 5818 (Figure S28). This result indicated that we clearly detected the signal of human mtDNA in mouse-derived receptor cells, confirming the successful transplantation of mitochondria, and the movement of nanomotors significantly promoted the cells to uptake more Mito/PC.

Further, primary hepatocytes were treated with different endocytosis inhibitors (4 °C (an energy inhibitor), cytochalasin D (an inhibitor of the micropinocytosis pathway), carbenoxolone (a gap junction blocker), chlorpromazine (an inhibitor of the clathrin-mediated pathway), and nystatin (an inhibitor of the caveolin-mediated pathway)) [55,56]. The main pathway of different samples into primary hepatocytes was explored by detecting the changes in cell uptake efficiency. As shown in Figure S29, the main pathway of Mito into hepatocytes may be energy-dependent and micropinocytosis and gap junction-mediated endocytosis. By contrast, for Mito/PC, carbenoxolone had little effect on the uptake efficiency, while chlorpromazine and nystatin treatments significantly inhibited the uptake efficiency (to 49.0% and 78.9% of the control group, respectively). Moreover, 4 °C and cytochalasin D also inhibited the cellular uptake of Mito/PC (to 42.3% and 70.5% of the control group, respectively). The results suggested that the main pathway of Mito/PC into primary hepatocytes may be the energy-dependent and clathrin- and caveolin-mediated endocytosis, and the micropinocytosis pathway. These mechanisms may facilitate the contact and fusion between exogenous mitochondria and host cell mitochondria.

Subsequently, both MitoTracker Red-labeled Mito and Mito/PC can co-locate with MitoTracker Green-labeled L-02 cells' own mitochondria (Figure 5a, d), suggesting that transplanted exogenous mitochondria may be able to fuse with the recipient cell's own mitochondria. We further investigated the recovery of energy metabolism of damaged hepatocytes after the administration of mitochondrial nanomotors. The viability of damaged primary hepatocytes decreased significantly, and the viability of cells after Mito/PC treatment was greatly increased and was greater than that after Mito treatment (Figure 5e), which may be related to the fact that primary hepatocytes captured more Mito/PC. Consistent with this trend, Mito/PC restored ATP supply to damaged hepatocytes, showing that the normalized ATP concentration can be recovered from 50.8% (pre-stimulated group) to 90.7% (Mito/PC group), comparable to that in the normal group (Figure 5f). Meanwhile, Mito/PC also restored the activity of mitochondrial respiratory chain complex I and complex V (increased from 0.26 to 1.30 U/$10^4$ cells, and from 0.02 to 0.12 U/$10^4$ cells, respectively), which was close to the normal level and worked better than Mito (Figure S30). Additionally, an important feature of damaged hepatocytes is a significant increase in ROS levels, and the transplantation of exogenous mitochondria can reduce ROS levels and thus reduce inflammation levels [22–24]. The total ROS content of cells was determined by 2′,7′-dichlorofluorescein diacetate (DCFH-DA, ROS probe) staining to explore the ROS removal ability of Mito/PC. The intracellular ROS fluorescence intensity was the strongest after pre-stimulated injury, and the intracellular ROS level could be reduced to a certain extent after Mito incubation, while Mito/PC had the best ability to remove ROS, and the fluorescence intensity was significantly reduced, about a quarter of that in the pre-stimulated group (Figure 5g, h and Figure S31). What's more, as shown in Figure S32, the pre-stimulated damaged cells maintained a high level of $O_2^-$ (approximately 0.06 μM). After incubation with Mito/PC for 3 h, the intracellular $O_2^-$ content decreased to 0.05 μM, and showed a significant and time-dependent decline with increasing incubation time. By 12 h of incubation, the $O_2^-$ content reached its lowest point, approaching the normal level. Meanwhile, the roundness of mitochondria was also evaluated, which can display mitochondrial morphology. The mean mitochondrial roundness returned to the normal levels after Mito/PC administration (Figure 5i, j). The above results indicated that mitochondrial transplantation can promote the recovery of key energy metabolic functions in damaged hepatocytes.

## 2.6 Ability of $SO_2$-releasing mitochondrial nanomotors to break through the capillarized sinusoids barrier and target fibrotic liver *in vivo*

The mitochondrial nanomotors constructed in this work showed a significant positive chemotactic effect on high concentrations of CDO and AST in hepatocytes *in vitro*, and were effectively captured by hepatocytes. As mentioned above, Mito/PC can target the sinusoids near the fibrotic site through chemotaxis, during which the L-cysteine in Mito/PC was catalyzed by enzymes to release $SO_2$. $SO_2$ can dilate blood vessels via the sGC/cGMP pathway [31,49], reverse the capillarized sinusoids and restore the fenestrated phenotype to facilitate therapeutic agents to break through the barrier and enter the Disse space to achieve effective targeting of the fibrotic site. To test this, we established a $CCl_4$-induced liver fibrosis mouse model. SEM images showed that, compared with the liver sinusoids of a normal mouse (with a porosity of 13.7%), the porosity in fibrotic liver decreased to 2.0%, indicating that the fenestrated phenotype disappeared (Figure 6a, b). After 24 h of treatment through the tail vein, the liver sections were frozen and stained with DEACA probe to evaluate the released $SO_2$. CLSM images showed that liver sections in the Mito/PC group showed a distinct blue fluorescence signal (representing $SO_2$), about 1.8 times that in the PBS group, while the blue fluorescence signal of Mito group had no significant change (Figure 6c, d), and there was no significant released $SO_2$ was observed in other organs (heart, spleen, lung and kidney) (Figure S33). Based on this, to evaluate the efficiency of $SO_2$-releasing mitochondrial nanomotors in breaking through the capillarized sinusoidal barrier, we used two-photon intravital microscopy to observe the distribution of samples and blood vessels in the liver 1.5 h after injecting the samples into the tail vein of mice with liver fibrosis. As shown in Figure 6g, h, and Figure S34, from the 2D fluorescence images and 3D reconstruction images, it can be observed that the green fluorescence representing Mito was still trapped within the red fluorescence representing blood vessels. Quantitative results also showed that the red and green fluorescence signals were completely colocalized, which may be due to the loss of permeability phenotype in the sinusoids, preventing unmodified mitochondria from breaking through the barrier and being easily metabolized by the liver. However, the green fluorescence signal representing Mito/PC was more abundant and mostly distributed outside the blood vessels, with a penetration depth of up to 5 μm. This may be because the released $SO_2$ restored the morphology and fenestrae of the sinusoids, facilitating the breakthrough of this barrier and the aggregation of mitochondrial nanomotors in the

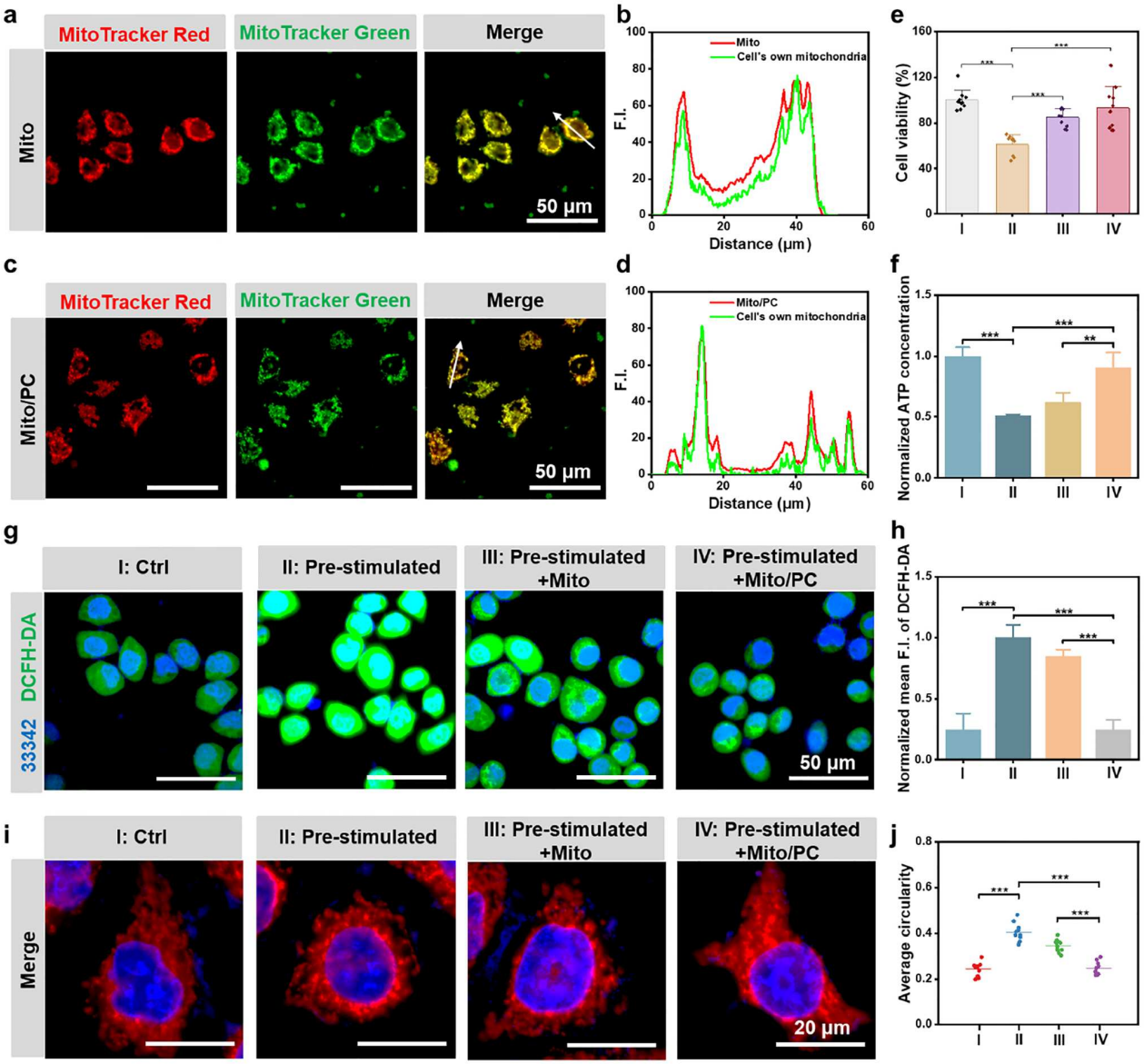



**Figure 5** (Color online) The ability of mitochondrial nanomotors to restore energy metabolism of damaged hepatocytes *in vitro*. (a) CLSM images and (b) intensity distribution along selected white lines of the co-localization of the cell's own mitochondria with Mito in L-02 cells. (c) CLSM images and (d) intensity distribution along selected white lines of the co-localization of the cell's own mitochondria with Mito/PC in L-02 cells (red, MitoTracker Red-labeled samples; green, MitoTracker Green-labeled cell's own mitochondria; blue, nucleus stained with Hoechst 33342). (e) Cell viability of primary hepatocytes incubated with different samples (I, Ctrl; II, pre-stimulated; III, pre-stimulated+Mito; IV, pre-stimulated+Mito/PC) for 12 h ($n$=10). (f) Intracellular normalized ATP concentration of L-02 cells incubated with different samples (I, Ctrl; II, pre-stimulated; III, pre-stimulated+Mito; IV, pre-stimulated +Mito/PC) ($n$=3). (g) Fluorescence images and (h) normalized fluorescence quantitative results of ROS changes in L-02 cells after different treatments (blue, nucleus stained with Hoechst 33342; green, ROS stained with DCFH-DA) ($n$=4). (i) CLSM images and (j) mitochondrial morphology analysis of L-02 cells after co-incubation with different samples for 6 h (red, intracellular mitochondria stained with MitoTracker Red; blue, nucleus stained with Hoechst 33342) ($n$=10). Experimental data are means ± SD of samples in a representative experiment. *$P$ < 0.05, **$P$ < 0.01, and ***$P$ < 0.001, determined by one-way ANOVA.

Disse space. These results indicated that $SO_2$-releasing mitochondrial nanomotors can significantly induce the formation of sinusoidal fenestrae and determine the time required to promote LSEC differentiation (within 1.5 h after intravenous injection *in vivo*).

Further, we used a $CCl_4$-induced liver fibrosis mouse model to verify whether this chemotactic behavior and rapid breakthrough of the liver sinusoids barrier could help mitochondrial nanomotors achieve effective liver targeting and retention *in vivo*. Firstly, *in vitro* imaging techniques were used to visually detect the fluorescence accumulation of samples in the fibrotic liver. After injection for 24 h, Mito/PC showed a strong fluorescent signal in the liver (Figure 6i), which was 2.2 times that in the Mito group (Figure 6j). The accumulation and biodistribution of different samples in the fibrotic liver were then analyzed by grinding the whole organ and measuring the total amount of the samples. As shown in Figure 6k, Mito/PC accumulation can increase to about 70.5% ID in fibrotic liver compared to that in the Mito group (56.2% ID), and was less distributed in other organs (Figure S35). In addition, fluorescence images showed that there was a certain accumulation of fluorescence in the liver after 6 h injection of Mito/PC. With the extension of injection time to 12 and 24 h, the fluorescence intensity of Mito/PC in the liver increased to 1.4 and 1.5 times, respectively (Figure 6l, m). Further, the specific proportion of Mito/PC in the liver can reach 68.6% ID (6 h), 67.7% ID (12 h) and 70.5% ID (24 h) (Figure 6n), while no significant accumulation of fluorescence was observed in other organs (Figure S36).

In addition, we characterized the chemotactic targeting ability of

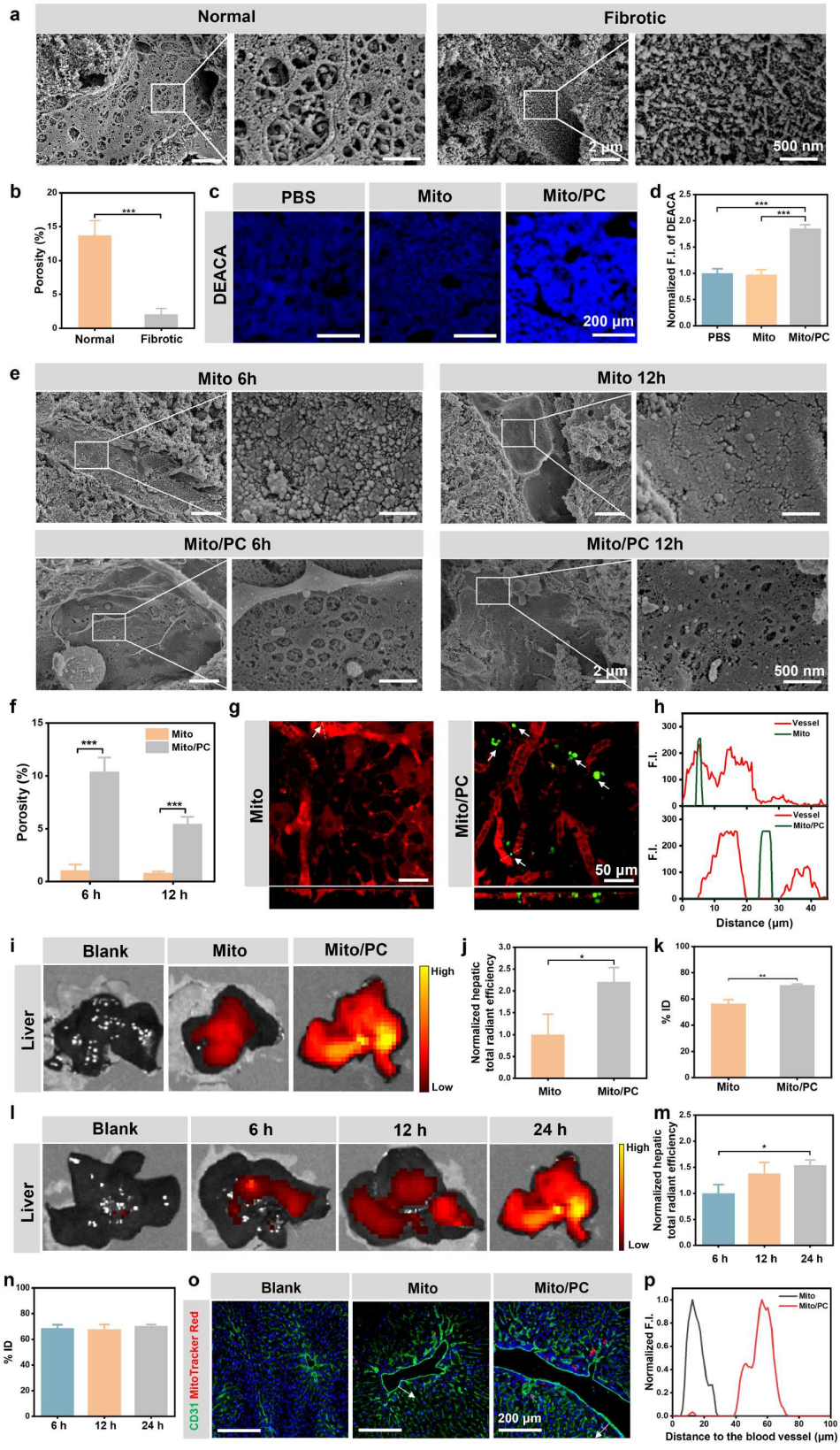



**Figure 6** (Color online) The ability of $SO_2$-releasing mitochondrial nanomotors to break through the capillarized sinusoidal barrier and target fibrotic liver *in vivo*. (a) SEM images of liver sinusoids morphology in normal or fibrotic mice. (b) Quantification of LSECs porosity from SEM images as shown in a ($n$=4). (c) Fluorescence images and (d) quantification results of released $SO_2$ in the liver after being treated with different samples (blue, $SO_2$ stained with DEACA) ($n$=3). (e) Representative SEM images of liver sinusoids morphology after different treatments. (f) Quantification of LSECs porosity from SEM images as shown in e ($n$=3). (g) Intravital 2D and 3D images of the distribution in the fibrotic liver treated with different samples for 1.5 h (green, samples stained with MitoTracker Red; red, vessels stained with FITC(GFP)). (h) Intensity distribution along selected lines (represented by white lines) of the colocalization of samples and blood vessels in the liver. (i) *Ex vivo* fluorescence images and (j) quantification results for the liver after being treated with different samples for 24 h. (k) Biodistribution of different samples quantified as % ID in liver ($n$=3). (l) *Ex vivo* fluorescence images and (m) quantification results for the liver after Mito/PC treatment for different times. (n) Biodistribution of Mito/PC at different times quantified as % ID in liver ($n$=3). (o) Fluorescence images and (p) intensity distribution along selected lines (represented by white lines) of the colocalization of samples and blood vessels in the liver (blue, nucleus stained with DAPI; red, MitoTracker Red-labeled samples; green, blood vessels stained with CD31). Experimental data are means ± SD of samples in a representative experiment. $^*P < 0.05$, $^{**}P < 0.01$, and $^{***}P < 0.001$, determined by one-way ANOVA or independent-samples $T$ test.

mitochondrial nanomotors in the TAA-induced cirrhosis model (Figure S37). Fluorescence images showed that, compared with other organs, the fluorescence accumulation intensity of Mito/PC in the liver was much stronger. Tissue homogenate data showed that the accumulation content of Mito/PC in the liver could reach 64.3% ID (6 h), 70.8% ID (12 h) and 70.8% ID (24 h), which was much higher than in other organs. In conclusion, compared with the mild liver fibrosis model, the speed and intensity of chemotactic targeting behavior of mitochondrial nanomotors in the severe liver fibrosis model showed no difference, and their ability to penetrate the thicker ECM barrier was not limited.

Finally, we investigated the tissue penetration of mitochondrial nanomotors in fibrotic livers (Figure 6o, p and Figure S38). Different samples labeled with MitoTracker Red were injected intravenously into fibrotic mice for 24 h, and then the livers were removed for immunofluorescence staining. It was observed that the red fluorescence representing Mito was more concentrated around the green fluorescence representing blood vessels, while the amount of red fluorescence penetrating into the liver tissue was less. Quantitative results also showed significant overlap or a mere 5 μm distance between the two fluorescence signals. In contrast, Mito/PC with chemotactic behavior appeared more frequently in liver tissues located farther from blood vessels, demonstrating better penetration with a depth of 20–40 μm. The above results indicated that mitochondrial nanomotors can achieve effective targeting, long-term accumulation, and deep penetration through chemotaxis in fibrotic livers, rapidly breaking through the capillarized sinusoidal barrier and further penetrating into the excessive ECM barrier.

## 2.7 Anti-fibrotic effect of $SO_2$-releasing mitochondrial nanomotors in $CCl_4$-induced liver fibrosis mouse model

To evaluate the therapeutic effect of $SO_2$-releasing mitochondrial nanomotors on breaking through the capillarized sinusoids barrier and over-deposited ECM barrier, as well as repairing damaged hepatocytes, we established a 6-week $CCl_4$-induced mild liver fibrosis mouse model. During the last two weeks, mice were administered three times a week with either phosphate buffer salts (PBS, II), Mito (IV), or Mito/PC (V) through the tail vein, or the clinical agent silymarin (SLB, III) by gavage, with normal mice as a healthy control group (I) (Figure 7a). All the fibrotic mice lost significantly more weight than healthy mice, but the fibrotic mice treated with Mito/PC had significantly improved liver indexes compared to the other treatment groups (Figure S39). Subsequently, we analyzed the serum liver function markers of mice in different treatment groups, and the results showed that compared with the PBS group, the serum AST, alanine aminotransferase (ALT) and total bilirubin (TBIL) levels of the Mito/PC group were reduced to close to the levels of a normal mouse (Figure S40). Besides, the serum inflammatory factor (IL-6 and TNF-α) levels can also be restored to normal levels (Figure S41).

We then evaluated the therapeutic efficacy of $SO_2$-releasing nanomotors in breaking through the capillarized sinusoids barrier and restoring the differentiated state of LSECs. SEM images showed that the quantity and porosity of sinusoids in the Mito/PC group significantly increased to 10.9%, which was close to the fenestrated phenotype of the normal mouse group, and significantly different from the capillarized phenotype of fibrotic liver in other treatment groups (Figure 7b, c). Further, we performed histopathological analyses of fibrotic liver in different treatment groups (Figure 7d). Hematoxylin and Eosin (H&E) staining showed extensive neutrophil inflammatory infiltration, hepatocyte contraction and death in the PBS group (the METAVIR score result was about A2, indicating moderate inflammatory activity) [57], compared to the normal group (the METAVIR score result was A0, indicating no inflammatory activity), while Mito/PC group showed a more normal histological structure and a significant reduction in the number of inflammatory lesions (the METAVIR score result was about A1, representing mild inflammatory activity) (Figure 7e). The activation of HSCs is also considered to be an important pathological feature of liver fibrosis, so the degree of HSC activation is also considered to be one of the indicators of the therapeutic effect of liver fibrosis. α-SMA (a marker for activated HSCs) immunohistochemical staining showed that the positive area of α-SMA in fibrotic liver after Mito/PC treatment was significantly reduced to 0.9%, compared with PBS (8.7%), SLB (5.3%) and Mito (3.5%) groups (Figure 7f) [11]. Liver sections were further stained with Masson's trichrome stain to assess collagen coverage and tissue fibrosis. As shown in Figure 7d, g, there were few collagen fibers in the healthy liver, while the fibrotic liver treated with PBS exhibited extensive collagen deposition (with a Masson-positive area reaching 6.4%). Compared to SLB (3.9%) and Mito (3.3%), the blue collagen in the liver treated with Mito/PC significantly decreased to 1.1%, approaching the level of normal liver. Consistent with this trend, hydroxyproline content in the fibrotic livers treated with Mito/PC was reduced more than in the other groups and was close to the level of normal liver (Figure 7h).

ROS immunofluorescence staining was performed on the liver sections of different treatment groups, and it was observed that the red fluorescence signal was the strongest in the PBS group, and the fluorescence signal of the Mito/PC treatment was significantly weakened, close to the level of normal liver, while the fluorescence signal of the Mito group decreased less (Figure 7i and Figure S42). Quantitative results showed a similar trend (Figure 7j). We also detected the contents of $O_2^-$, hydrogen peroxide ($H_2O_2$) and superoxide dismutase (SOD) in fibrotic liver. The results showed that compared with other treatment groups, the contents of $O_2^-$ and $H_2O_2$ in the Mito/PC group were significantly decreased (Figure 7k, l), and the content of SOD was increased (Figure 7m), which was close to the level of normal liver. In addition, TEM images of liver mitochondria showed reduced mitochondrial swelling, fracture, and ridge loss in hepatocytes after Mito/PC treatment (Figure 7n).

## 2.8 Therapeutic effect of $SO_2$-releasing mitochondrial nanomotors in a TAA-induced severe liver fibrosis mouse model

The above results confirmed that mitochondrial nanomotors can effectively alleviate the outcomes of $CCl_4$-induced fibrosis (the fibrosis rating was about F1/2 stage) (Figure S43). However, since both the establishment of the model and the treatment process required the continuous stimulation of the chemical poison $CCl_4$ [17,58,59], it was difficult to judge whether the treatment of mitochondrial nanomotors can prevent the progression of liver fibrosis. We therefore established a 12-week mouse model of TAA-induced severe liver fibrosis (cirrhosis model, the fibrosis stage was about F3) without continuous stimulation of TAA during the treatment process to investigate whether mitochondrial nanomotors could prevent the progression of liver fibrosis (Figure 8a) [60].

We observed the inhibition of mitochondrial respiratory chain complex I and V activity in cirrhotic liver compared to normal liver (complex I decreased from 406.3 to 163.6 U $g^{-1}$, and complex V decreased from 417.5 to 153.2 U $g^{-1}$), demonstrating significant mitochondrial damage. After Mito/PC treatment, the activity of mitochondrial complex I and complex V was effectively restored to 463.4 and 367.3 U $g^{-1}$, close to normal liver levels (Figure 8b, c). The levels of inflammatory factors in the livers after Mito/PC

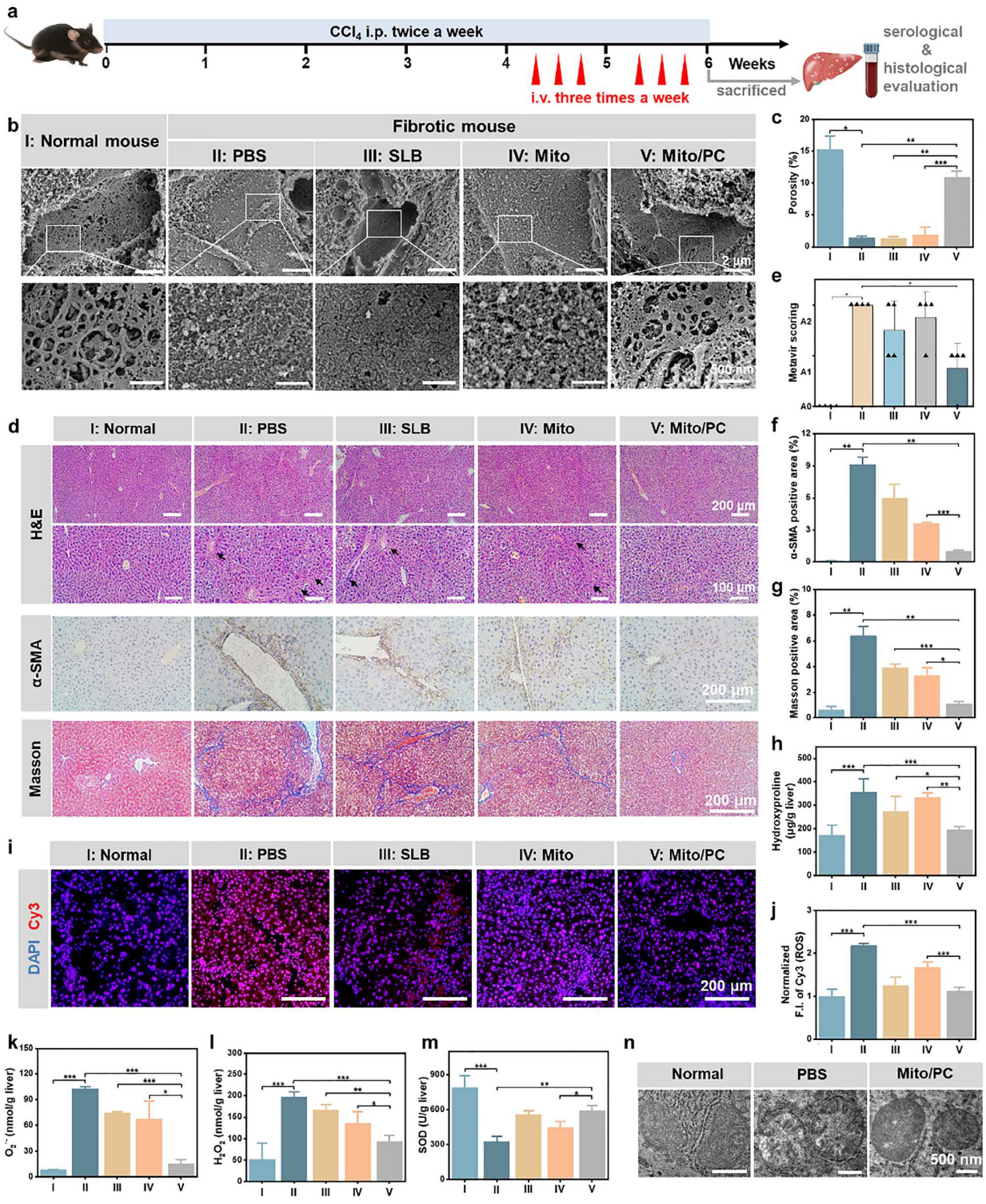



**Figure 7** (Color online) *In vivo* therapeutic effect of mitochondrial nanomotors in a $CCl_4$-induced liver fibrosis mouse model. (a) Schematic illustration of the establishment of the $CCl_4$-induced liver fibrosis model and the tail vein injection of therapeutic agents in C57BL/6 mice. (b) SEM images of liver sinusoids after different treatments. (c) Quantification of porosity from SEM images as shown in b ($n$=4). (d) Representative photomicroscope images of liver sections in different treatments stained with H&E staining, α-SMA immunohistochemical staining and Masson trichrome staining. Quantification of (e) Metavir scoring of damage status, (f) α-SMA positive area and (g) Masson's trichrome-stained fibrotic area ($n$=4). (h) Hydroxyproline of fibrotic liver with different treatments ($n$=4). (i) Immunofluorescence images and (j) corresponding normalized fluorescence of ROS ($n$=3). Quantification of liver (k) $O_2^-$ ($n$=4), (l) $H_2O_2$ ($n$=4) and (m) SOD ($n$=3) (I, Normal; II, PBS; III, SLB; IV, Mito; V, Mito/PC). (n) Representative TEM images of mitochondrial morphology of liver after different treatments. Experimental data are means ± SD of samples in a representative experiment. $^*P < 0.05$, $^{**}P < 0.01$, and $^{***}P < 0.001$, determined by one-way ANOVA and nonparametric tests.

treatment could be restored to near normal levels (IL-6 decreased from 57.0 to 36.7 pg $mL^{-1}$ while TNF-α decreased from 472.4 to 161.7 pg $mL^{-1}$) (Figure 8d, e). The above results showed that transplanted mitochondrial nanomotors can effectively restore the energy supply of the liver and reduce the inflammation level. Then, TdT-mediated dUTP nick end labeling (TUNEL) staining was performed on liver sections after different treatments to assess the extent of liver deterioration (Figure 8f, g). The TAA-induced model

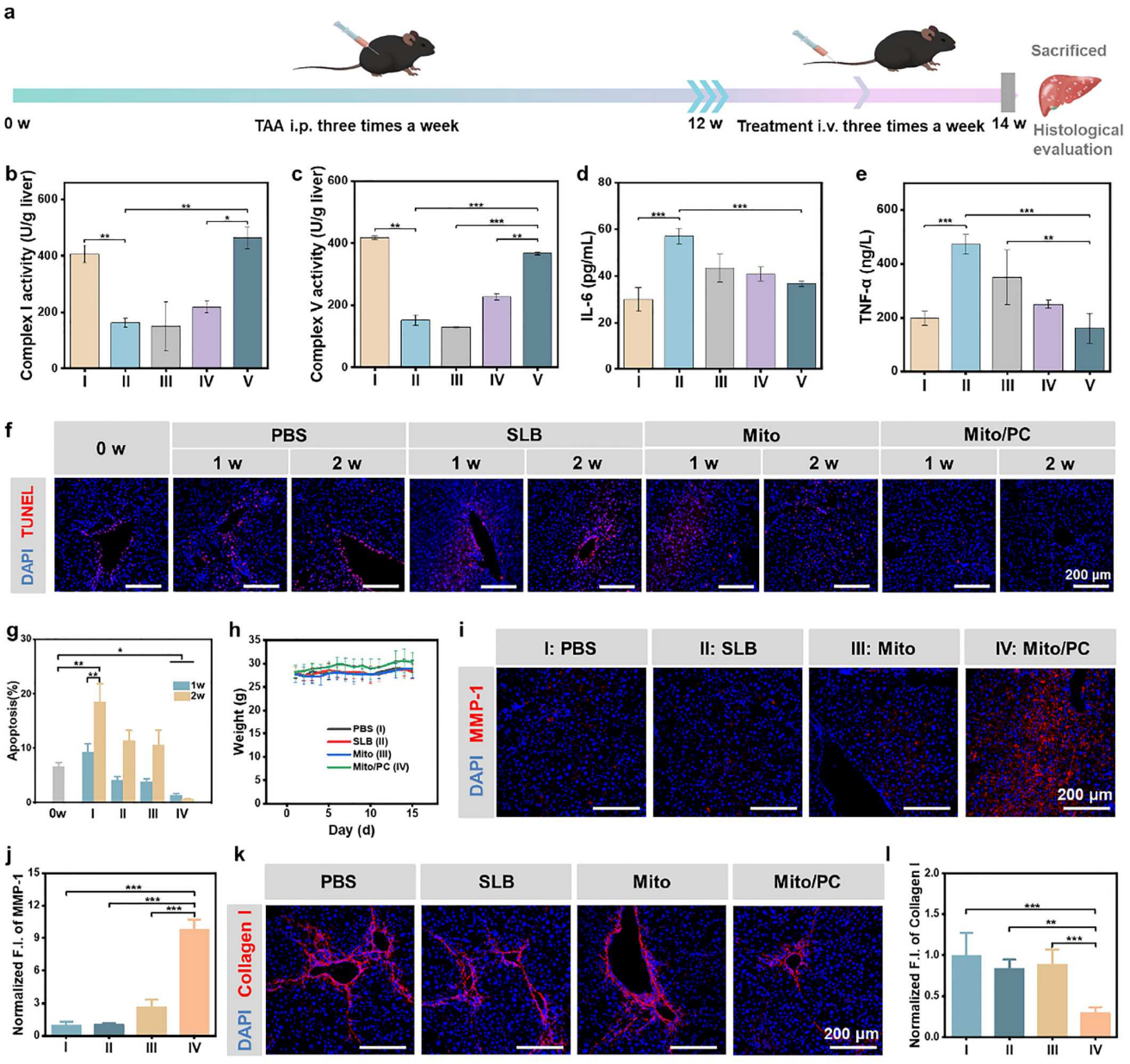



**Figure 8** (Color online) *In vivo* therapeutic effect of $SO_2$-releasing mitochondrial nanomotors in a TAA-induced liver fibrosis mouse model. (a) Schematic illustration of the establishment and treatment of the TAA-induced liver fibrosis model. The activity of (b) complex I and (c) complex V of livers with different treatments ($n$=3). (d) IL-6 and (e) TNF-α levels of livers with different treatments ($n$=3). (f) Representative images and (g) apoptosis of TUNEL staining of livers with different treatments ($n$=3). (h) Weight changes in mice over two weeks of treatment. (i) Immunofluorescence staining images and (j) normalized quantitative analysis of MMP-1 ($n$=4). (k) Immunofluorescence staining images and (l) normalized quantitative analysis of collagen I ($n$=4) (I, PBS; II, SLB; III, Mito; IV, Mito/PC). Experimental data are means ± SD of samples in a representative experiment. $^*P < 0.05$, $^{**}P < 0.01$, and $^{***}P < 0.001$, determined by one-way ANOVA.

(treatment for 0 weeks) induced hepatocyte apoptosis (about 6.6%). After 1 and 2 weeks of PBS treatment, hepatocyte apoptosis increased (about 9.2% and 18.5%, respectively), indicating that the hepatocyte damage was still sustained and the fibrosis process was still developing. After 1 week of Mito/PC treatment, the cell apoptosis was reduced to 1.3%, which was significantly lower than that in the PBS (9.2%), SLB (4.1%) and Mito (3.8%) groups, indicating that mitochondrial transplantation promoted by nanomotors can effectively repair damaged hepatocytes and protect hepatocytes from apoptosis. With the increase in treatment to 2 weeks, Mito/PC was still able to effectively prevent hepatocyte apoptosis (about 0.7%), while the degree of apoptosis in the SLB (11.3%) and Mito group (10.6%) was aggravated, and fibrosis continued to worsen. These results indicated that mitochondrial transplantation can effectively repair damaged hepatocytes, reduce hepatocyte apoptosis, and prevent liver fibrosis progression. The weight records during the treatment showed that the weight of mice in the Mito/PC group gradually increased and was significantly higher than that in the other groups (Figure 8h), which may be because mitochondrial transplantation can prevent the continuous deterioration of liver fibrosis.

We further explored whether $SO_2$ released by mitochondrial nanomotors can break through the ECM barrier by activating endogenous pathways in this model. Studies have shown that $SO_2$ can stimulate the production of NO [33–35], which can react with ROS to form peroxynitrite to stimulate the production of MMP-1, thereby degrading the collagen components in the ECM. 3-Nitrotyrosine (3-NT) (a biomarker of peroxynitrite) immunohis-

tochemical staining [35] showed that the expression of 3-NT was weak in the fibrosis group (PBS group), whereas obvious brown staining (representing 3-NT) was observed in the Mito/PC group, with a positive area of 11.9%, indicating increased peroxynitrite production. However, the 3-NT levels in the Mito group (0.7%) and SLB group (0.4%) were similar to those in the PBS group (0.5%) (Figure S44). Then, MMP-1 and type I collagen immunofluorescence staining showed that MMP-1 expression was weak in the fibrosis group (PBS group), while collagen I expression was significant. However, the MMP-1 red fluorescence signal in Mito/PC group was significantly enhanced, which was 9.8 times that of fibrosis group (Figure 8i, j and Figure S45), and the fluorescence signal of type I collagen decreased significantly to 29.8% of the fibrotic group (Figure 8k, l and Figure S46), while the levels of MMP-1 and type I collagen in Mito and SLB groups were similar to that of the fibrotic group. The results showed that $SO_2$-releasing mitochondrial nanomotors promoted the degradation of type I collagen by increasing the activity of MMP-1, thus breaking through the ECM barrier.

Finally, we performed transcriptome sequencing on the liver tissues of TAA-induced cirrhotic mice after treatment. Compared to the PBS group, the Mito/PC group showed 395 significantly downregulated DEGs and 146 upregulated DEGs. Gene ontology (GO)-based functional enrichment analysis and Kyoto Encyclopedia of Genes and Genomes (KEGG) pathway enrichment analysis revealed that, compared to the PBS group, the downregulated genes in the liver after Mito/PC treatment were primarily involved in the response to wounding and ribosome biogenesis related to protein synthesis [4,61]. Additionally, genes associated with inflammatory signaling pathways (such as TNF, MAPK, and IL-17 signaling pathways) were downregulated [62–64]. Since cell cycle arrest represent a vital role in the prevention of hepatocytes and maladaptive repair following hepatocellular injury, avoiding replication of damaged DNA and carcinogenesis [24,65], the downregulation of cell proliferation-related genes-including those involved in the positive regulation of cell proliferation, P53 signaling pathway, and microRNAs in cancer-suggested that maladaptive repair in the liver was suppressed after treatment in the Mito/PC group [66] (Figure 9a). After Mito/PC treatment, the upregulated genes in the liver were associated with key intermediates of the mitochondrial tricarboxylic acid cycle, such as succinate transmembrane transport and α-ketoglutarate transmembrane transporter activity [62,67]. Additionally, genes related to xenobiotic metabolic activity and liver protective mechanisms were upregulated, including 3′-phosphoadenosine 5′-phosphosulfate metabolism and cytochrome P450-mediated metabolism of xenobiotics. Furthermore, the Mito/PC treatment rescued various metabolic processes in liver cells, including nitrogen metabolism, bile acid synthesis and secretion, and carbohydrate metabolism (Figure 9b and Figures S47 and S48) [24]. Subsequently, we compared the DEGs between the Mito group and the Mito/PC group. Compared to the Mito group, the Mito/PC group showed 730 downregulated and 273 upregulated DEGs. In the Mito/PC-treated liver, genes related to immune responses (including chemokine-chemokine receptor interactions and NOD-like receptor signaling pathways) and inflammatory responses (such as NF-κB, TNF, MAPK, and IL-17 signaling pathways) were downregulated compared to the Mito group. Additionally, genes associated with cell proliferation (*e.g.*, the P53 signaling pathway) were also downregulated (Figure 9c). The upregulated DEGs in the Mito/PC group were involved in various cellular metabolic processes, including tryptophan metabolism, retinol metabolism, steroid metabolism, and cytochrome P450-mediated xenobiotic metabolism (Figure 9d and Figures S49 and S50). In summary, the mitochondrial nanomotors can comprehensively improve mitochondrial-related functions and cellular metabolic functions at the transcriptional level, demonstrating promising therapeutic effects.

### 2.9 Biosafety evaluation of mitochondrial nanomotors

The biosafety of mitochondrial nanomotors was evaluated in detail. Hemolysis test results showed that Mito and Mito/PC had good blood compatibility (Figure S51). For healthy mice, with the injection time extended to 48 and 72 h, almost no obvious fluorescence signal of Mito/PC was observed in the major organs (Figure S52), suggesting that the nanomotor coating can be completely metabolized *in vivo*. Further, after 7 days of injection in normal mice, biochemical analysis results indicated that liver function indicators (ALT and AST) were normal. H&E staining of liver tissues showed no inflammatory infiltration or morphological changes, and SEM images revealed the normal fenestrated structure of liver sinusoids (Figure S53). For liver fibrosis mice, within the observed period in the $CCl_4$-induced liver fibrosis model (2 weeks of treatment, with a total of 6 administrations), H&E staining results indicated that the treatment with nanomotors caused no significant pathological changes in the major organs, including heart, spleen, lungs and kidneys (Figure S54) [68]. The above results indicated that mitochondrial nanomotors had no obvious toxicity to healthy liver tissues and possessed good biosafety.

## 3 Discussion

From the point of view of disease treatment, this work not only underscores the pivotal role of mitochondrial transplantation in halting the advancement of liver fibrosis but also introduces a novel strategy that surmounts the two pathological hurdles to effectively deliver mitochondria to the site of fibrosis. Most existing studies that address these dual barriers usually employ a sequential drug delivery approach: one drug is administered for two weeks to breach the first barrier, followed by a second drug for another two weeks to overcome the second barrier [17]. Alternatively, the first drug is injected first, and the second drug is injected 1 day later, and the treatment is carried out as a cycle. For example, Nie *et al.* [58] first administered the sGC stimulator riociguat twice within 48 h to open capillarized liver sinusoids. During the second administration of riociguat, they simultaneously injected peptide nanoparticles encapsulating the anti-fibrotic agent JQ1 and targeting HSCs. This treatment cycle was repeated over two weeks, which promoted the transport of nanoparticles across the sinusoidal endothelial wall and enhanced their accumulation in the Disse space. Similarly, Jiang *et al.* [59] first injected nanoparticles loaded with the drug vismodegib and targeting LSECs to normalize the LSEC phenotype. 24 h later, they injected nanoparticles loaded with silibinin and targeting hepatocytes to alleviate oxidative stress. This treatment cycle was also repeated over two weeks. However, the dynamic liver microenvironment introduces timing and uncertainty in the reversal of capillarized liver sinusoids, which may hinder the second drug from crossing the sinusoids to reach the Disse space and penetrate deeply, significantly diminishing its efficacy. At present, there are few reports of drug delivery systems simultaneously overcoming the dual pathological barriers. In contrast, the $SO_2$-released nanomotors proposed in this work can achieve this goal. By utilizing the nature of the gas signaling molecule $SO_2$ to regulate the endogenous pathways [69], the mitochondrial nanomotors can promote the mitochondrial nanomotors to enter the ECM barrier while almost simultaneously ensuring the opening of liver sinusoids, and further exert their effectiveness. This strategy provides an innovative idea for overcoming the double pathological

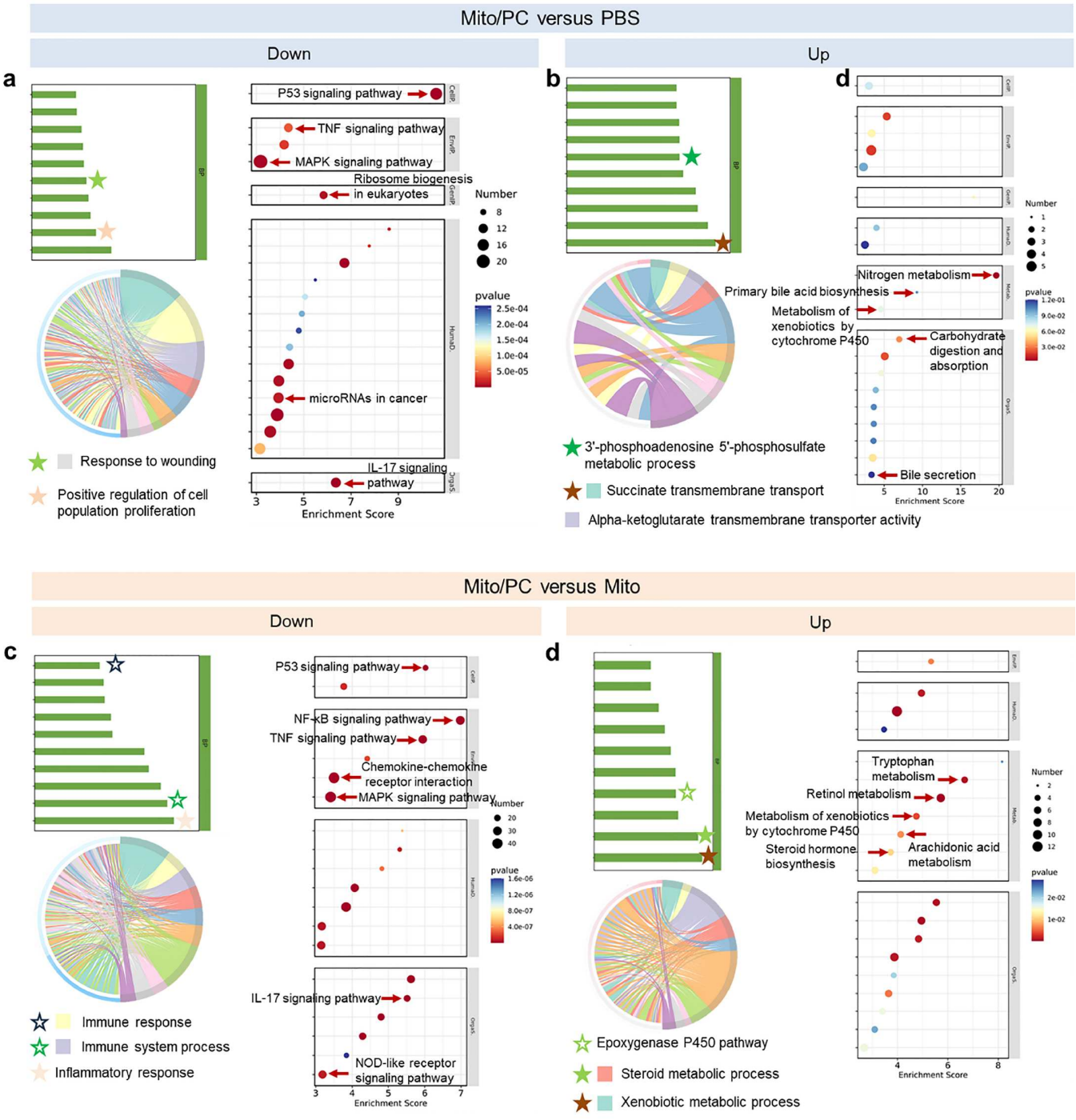



**Figure 9** (Color online) Transcriptomics analysis in the TAA-induced liver cirrhosis model. GO and KEGG pathway enrichment analysis showing DEGs (a, b) in the Mito/PC group compared with the PBS group, (c, d) in the Mito/PC group compared with the Mito group ($n$=3). Histogram: top ten significantly enriched biological processes. The horizontal axis represents the −log10 ($P$) of the pathway and the vertical axis represents the GO terms. Chord diagram: top ten significantly enriched GO terms, in which the right semicircle represents the names of ten GO terms, and the left semicircle represents DEGs in GO terms. The color map represents the fold-change of genes (log2 scale), and the colored bands connect a gene to a specific GO term. Bubble diagram: the top 20 significantly enriched KEGG terms. The horizontal axis represents the enrichment score, the vertical axis represents the description and bubble sizes represent enriched gene counts.

barriers in the liver fibrosis microenvironment.

From the perspective of mitochondrial transplantation in the treatment of liver metabolic diseases, factors such as oxidative stress and metabolic disorders related to mitochondrial dysfunction are involved in the pathogenesis of these diseases [19], so the repair of mitochondrial homeostasis is expected to have potential therapeutic effects on these diseases and their complications, and exogenous supplementation of healthy mitochondria is becoming a promising treatment method [70]. So far, four studies have reported this strategy. In 2017, Fu *et al.* [22] used mitochondria isolated from hepatocarcinoma cells as a mitochondrial therapeutic agent administered intravenously to treat mouse fatty liver induced by high-fat diets. This is the first reported case of the mitochondrial system being used to treat liver disease in animals. Subsequently, the team demonstrated that hepatocarcinoma cells-derived mitochondria, administered intravenously, could effectively treat acetaminophen-induced liver damage in mice [23]. In 2020, the team demonstrated at the transcriptional level that healthy mouse

liver-derived mitochondria can upregulate the transcriptional activation of genes associated with mitochondrial function, providing a new approach for treating $CCl_4$-induced liver damage [24]. In the same year, Liu's team [71] reported for the first time the specific transplantation of mitochondria-protein complexes into living animal liver cells via a simple peripheral intravenous injection. In contrast, the mitochondrial transplantation method constructed in this work has considerable advantages in the treatment of liver metabolic diseases with the support of nanomotor technology. The introduction of nanomotor technology can not only protect mitochondrial activity from oxidative stress in the disease microenvironment, but also make mitochondria efficiently chemotactic targets to the damaged liver under the action of the CDO/AST enzyme concentration gradient field, further breaking through the double pathological barriers. Thus, nanomotors enable mitochondria to not only "reach" the damaged liver, but also "penetrate" into the damaged liver, which is not possible with unmodified mitochondria and mitochondria-protein complexes injected intravenously.

From the perspective of $SO_2$ donors, the unique physiological effect of $SO_2$ and its derivatives in lowering rat blood pressure by relaxing blood vessels has been revealed since 2003 [72]. Donors that can release $SO_2$ in the body environment, including inorganic salts (sulfites and bisulfites), small molecule donors (compounds with sulfinyl groups), or large molecule donors (prodrug polymers containing sulfinyl groups), have been developed [73]. However, most of the current donors face the issue of a lack of disease tissue-selective release of $SO_2$. In contrast, this paper proposes a new form of $SO_2$ donor specifically targeting the microenvironment of liver fibrosis. This approach can not only specifically respond to damaged livers by releasing $SO_2$ but also does not produce significant toxicity to normal tissues, providing an innovative idea for enriching the forms of $SO_2$ donors. The introduction of nanomotor technology can fully leverage the physiological effects of $SO_2$, such as its vasodilatory properties that activate endogenous signaling pathways and play an important role in breaking through the capillary-like liver sinusoidal barrier, showing a certain degree of innovation in the treatment of liver fibrosis.

From the perspective of allogeneic transplantation, in fact, many studies on mitochondrial transplantation currently opt for allogeneic transplantation to avoid the difficulties and additional damage to patients associated with the extraction of autologous cellular mitochondria. For example, mitochondria derived from adult cardiac fibroblasts have been transplanted into the ischemic hearts of rabbits [74], mitochondria from human-induced pluripotent stem cell-derived cardiomyocytes have been transplanted into mice with myocardial infarction [75], and mitochondria from the human liver cancer cell line HepG2 have been transplanted into mice with non-alcoholic fatty liver disease and mice with acetaminophen-induced liver injury [22,23]. In this study, we chose to transplant mitochondria derived from huMSCs into mice with liver fibrosis because they possess high proliferative capacity and a relatively young cellular state [76]. Mitochondria from younger-state cells may have a superior ability to improve cellular function. huMSCs are the most immunocompatible cells in stem cell-based therapies [76]. In the long term, we hope that these huMSCs-derived mitochondria could be used for the treatment of human liver fibrosis. Additionally, researchers have used huMSCs-derived mitochondria to achieve repair of traumatic brain injury and peripheral nerve injury in rat models [77]. Since it is not the transplantation of whole cells, allogeneic mitochondrial transplantation generally does not exhibit a significant rejection reaction [77]. Our experimental data also indicated that in these studies involving allogeneic mitochondrial transplantation, no late immune or inflammatory responses to the transplanted mitochondria seem to have been observed. All procedures involving animals were performed in full compliance with the National Institutes of Health guidelines for laboratory animal care and use. The experimental protocol was reviewed and approved by the Animal Experiment Ethics Committee of Nanjing Normal University (Approval No. IACUC-2024274).

## 4 Conclusions

In summary, this work proposed a method to transplant mitochondria to the liver using $SO_2$-releasing nanomotors for the treatment of liver fibrosis. The modification of $SO_2$-releasing nanomotors enabled mitochondria to chemotactically target the fibrotic sites with high concentrations of CDO and AST. In particular, the released $SO_2$ can effectively restore the fenestrated phenotype of LSECs by enhancing cGMP expression and decreasing $Ca^{2+}$ levels, and promote mitochondrial nanomotors to break through the capillarized sinusoids within 1.5 h and the ECM barrier. The fibrotic area was significantly reduced from 6.3% to 1.1%. After successfully navigating the dual pathological barriers, the targeting efficiency of the mitochondrial nanomotors soared to approximately 70.5% ID, significantly outperforming unmodified mitochondria, which achieved only 56.2% ID. The transplanted mitochondria can effectively repair the damaged hepatocyte and significantly reduce apoptosis, and maintain this level during the 2-week treatment (with an apoptosis ratio of about 1.0%), while the degree of apoptosis in the fibrosis group continued to increase (apoptosis ratio increased to 18.5%). Further, the mitochondrial nanomotors can comprehensively improve mitochondrial-related functions and cellular metabolic functions at the transcriptional level. This strategy of mitochondrial transplantation provides innovative insights and holds significant promise for halting the progression of liver fibrosis, rather than merely providing palliative care or temporary relief.

### Conflict of interest

The authors declare no conflict of interest.


### Acknowledgement

The work was supported by the National Natural Science Foundation of China (NSFC) (52422306), the Excellent Young Scholars (NSFC) (22275095, 22175096, 22475103), the Jiangsu Key Laboratory of Biofunctional Materials, the Jiangsu Collaborative Innovation Center of Biomedical Functional Materials and the Postgraduate Research & Practice Innovation Program of Jiangsu Province (KYCX25_1941).


### Supporting information

The supporting information is available online at http://chem.scichina.com and http://link.springer.com/journal/11426. The supporting materials are published as submitted, without typesetting or editing. The responsibility for scientific accuracy and content remains entirely with the authors.

### References


1 Asrani SK, Devarbhavi H, Eaton J, Kamath PS. *J Hepatol*, 2019, 70: 151–171
2 Gilgenkrantz H, Paradis V, Lotersztajn S. *Hepatology*, 2025, 81: 269–287
3 Kisseleva T, Brenner D. *Nat Rev Gastroenterol Hepatol*, 2020, 18: 151–166
4 Friedman SL. *Gastroenterology*, 2008, 134: 1655–1669
5 Begriche K, Massart J, Robin MA, Borgne-Sanchez A, Fromenty B. *J Hepatol*, 2011, 54: 773–794
6 Tilg H, Moschen AR. *Hepatology*, 2010, 52: 1836–1846
7 Gao B, Bataller R. *Gastroenterology*, 2011, 141: 1572–1585
8 Mota M, Banini BA, Cazanave SC, Sanyal AJ. *Metabolism*, 2016, 65: 1049–1061
9 Chen P, Yao L, Yuan M, Wang Z, Zhang Q, Jiang Y, Li L. *Genes Dis*, 2024, 11: 101115
10 DeLeve LD. *Hepatology*, 2015, 61: 1740–1746
11 Pinzani M, Rombouts K, Colagrande S. *J Hepatol*, 2005, 42: S22–S36
12 Chen L, Duan Y, Jiang T, Mao C, Zhu X, Wan M. *Sci Bull*, 2024, 69: 1829–1832
13 Guo YC, Lu LG. *J Clin Transl Hepatol*, 2020, 8: 1–9
14 Zhao L, Tang H, Cheng Z. *Pharmaceuticals*, 2024, 17: 1724
15 Chen L, Guo W, Mao C, Shen J, Wan M. *J Mater Chem B*, 2024, 12: 1446–1466
16 Yuan Y, Li J, Chen M, Zhao Y, Zhang B, Chen X, Zhao J, Liang H, Chen Q. *J Control Release*, 2024, 376: 318–336

17 Zhang LF, Wang XH, Zhang CL, Lee J, Duan BW, Xing L, Li L, Oh YK, Jiang HL. *ACS Nano*, 2022, 16: 14029–14042
18 Böttcher K, Pinzani M. *Adv Drug Deliver Rev*, 2017, 121: 3–8
19 Mansouri A, Gattolliat CH, Asselah T. *Gastroenterology*, 2018, 155: 629–647
20 Zhang IW, López-Vicario C, Duran-Güell M, Clària J. *Front Mol Biosci*, 2021, 8: 772174
21 Lee H, Lee TJ, Galloway CA, Zhi W, Xiao W, de Mesy Bentley KL, Sharma A, Teng Y, Sesaki H, Yoon Y. *Nat Commun*, 2023, 14: 6721
22 Fu A, Shi X, Zhang H, Fu B. *Front Pharmacol*, 2017, 8: 241
23 Shi X, Bai H, Zhao M, Li X, Sun X, Jiang H, Fu A. *Transl Res*, 2018, 196: 31–41
24 Zhao Z, Hou Y, Zhou W, Keerthiga R, Fu A. *Bioeng Transla Med*, 2021, 6: e10209
25 Sun X, Gao R, Li W, Zhao Y, Yang H, Chen H, Jiang H, Dong Z, Hu J, Liu J, Zou Y, Sun A, Ge J. *Bioactive Mater*, 2021, 6: 2058–2069
26 Joseph CA, Maroney MJ. *Chem Commun*, 2007, 32: 3338–3349
27 Pol S, Nalpas B, Vassault A, Bousquet-Lemercier B, Franco D, Lacour B, Berthelot P, Hanoune J, Barouki R. *Hepatology*, 1991, 14: 620–625
28 Parsons RB, Ramsden DB, Waring RH, Barber PC, Williams AC. *J Hepatol*, 1998, 29: 595–602
29 Wang XB, Du JB, Cui H. *Eur J Pharmacol*, 2015, 764: 94–99
30 Li W, Li Y, Jiang X, Li X, Yu Z. *Molecules*, 2018, 23: 2378
31 Huang Y, Zhang H, Lv B, Tang C, Du J, Jin H. *Antioxid Redox Signal*, 2022, 36: 256–274
32 Gracia-Sancho J, Caparrós E, Fernández-Iglesias A, Francés R. *Nat Rev Gastroenterol Hepatol*, 2021, 18: 411–431
33 Li W, Tang C, Jin H, Du J. *Atherosclerosis*, 2011, 215: 323–330
34 Li J, Li R, Meng Z. *Eur J Pharmacol*, 2010, 645: 143–150
35 Wan MM, Chen H, Da Wang Z, Liu ZY, Yu YQ, Li L, Miao ZY, Wang XW, Wang Q, Mao C, Shen J, Wei J. *Adv Sci*, 2020, 8: 2002525
36 Wu Z, Chen L, Guo W, Wang J, Ni H, Liu J, Jiang W, Shen J, Mao C, Zhou M, Wan M. *Nat Nanotechnol*, 2024, 19: 1375–1385
37 Chen W, Huang T, Shi K, Chu B, Qian Z. *Nano Today*, 2020, 35: 100966
38 Prasad BB, Jauhari D, Tiwari MP. *Biosens Bioelectron*, 2014, 59: 81–88
39 Tian Y, Zheng J, Tang X, Ren Q, Wang Y, Yang W. *Part Part Syst Charact*, 2015, 32: 547–551
40 Chen H, Li T, Liu Z, Tang S, Tong J, Tao Y, Zhao Z, Li N, Mao C, Shen J, Wan M. *Nat Commun*, 2023, 14: 941
41 Smiley ST, Reers M, Mottola-Hartshorn C, Lin M, Chen A, Smith TW, Steele Jr GD, Chen LB. *Proc Natl Acad Sci USA*, 1991, 88: 3671–3675
42 Sivandzade F, Bhalerao A, Cucullo L. *Bio-protocol*, 2019, 9: e3128
43 Lanza IR, Nair KS. *Methods Enzymol*, 2009, 457: 349–372, doi: 10.1016/s0076-6879(09)05020-4
44 An L, Zhang P, Shen W, Yi X, Yin W, Jiang R, Xiao C. *Bioactive Mater*, 2021, 6: 1365–1374
45 Li H, Li Y, Liu J, He Q, Wu Y. *Nanoscale*, 2022, 14: 7444–7459
46 Dunderdale G, Ebbens S, Fairclough P, Howse J. *Langmuir*, 2012, 28: 10997–11006
47 Ma X, Jannasch A, Albrecht UR, Hahn K, Miguel-López A, Schäffer E, Sánchez S. *Nano Lett*, 2015, 15: 7043–7050
48 Li T, Liu Z, Hu J, Chen L, Chen T, Tang Q, Yu B, Zhao B, Mao C, Wan M. *Adv Mater*, 2022, 35: 2305226
49 Yao Q, Huang Y, Liu AD, Zhu M, Liu J, Yan H, Zhang Q, Geng B, Gao Y, Du S, Huang P, Tang C, Du J, Jin H. *Am J Physiol-Regulatory Integr Comp Physiol*, 2016, 310: R1073–R1080
50 Sanyal AJ, Mirshahi F. *Hepatology*, 1999, 29: 710–718
51 Wei Z, Lei J, Shen F, Dai Y, Sun Y, Liu Y, Dai Y, Jian Z, Wang S, Chen Z, Liao K, Hong S. *Adv Sci*, 2020, 7: 2000963
52 Tu Y, Peng F, Wilson DA. *Adv Mater*, 2017, 29: 1701970
53 Xie G, Kanel GC, DeLeve LD. *Gastroenterology*, 2010, 138: S-773
54 Fan QQ, Zhang CL, Qiao JB, Cui PF, Xing L, Oh YK, Jiang HL. *Biomaterials*, 2020, 230: 119616
55 Chen H, Shi T, Wang Y, Liu Z, Liu F, Zhang H, Wang X, Miao Z, Liu B, Wan M, Mao C, Wei J. *J Am Chem Soc*, 2021, 143: 12025–12037
56 Bhattacharya D, Slavin MB, Hood DA. *Am J Physiol Cell Physiol*, 2023, 325: C862–C884
57 Han X, Gong N, Xue L, Billingsley MM, El-Mayta R, Shepherd SJ, Alameh MG, Weissman D, Mitchell MJ. *Nat Commun*, 2023, 14: 75
58 Li F, Zhao Y, Cheng Z, Wang Y, Yue Y, Cheng X, Sun J, Atabakhshi-Kashi M, Yao J, Dou J, Yu J, Zhang X, Qi Y, Li X, Qi X, Nie G. *Adv Mater*, 2023, 35: 2212206
59 Zhang L, Deng W, Huang Q, Zhang J, Wang Y, Zhou T, Xing L, Jiang H. *Adv Mater*, 2024, 36: 2311474
60 Zhang J, Shen H, Xu J, Liu L, Tan J, Li M, Xu N, Luo S, Wang J, Yang F, Tang J, Li Q, Wang Y, Yu L, Yan Z. *ACS Nano*, 2020, 14: 6305–6322
61 Luo W, Zhou J, Yan Y, Xu X. *Genes Dis*, 2025, 12: 101512
62 Zhang T, Hu J, Wang X, Zhao X, Li Z, Niu J, Steer CJ, Zheng G, Song G. *J Hepatol*, 2019, 70: 87–96
63 Fang Z, Xu H, Duan J, Ruan B, Liu J, Song P, Ding J, Xu C, Li Z, Dou K, Wang L. *Sig Transduct Target Ther*, 2023, 8: 94
64 Meng F, Wang K, Aoyama T, Grivennikov SI, Paik YH, Scholten D, Cong M, Iwaisako K, Liu X, Zhang M, Österreicher CH, Stickel F, Ley K, Brenner DA, Kisseleva T. *Gastroenterology*, 2012, 143: 765–776.e3
65 Wang W, Sun W, Gao B, Lian X, Zhou H. *Curr Protein Pept Sci*, 2017, 18: 1224–1231
66 Kim J, Lee C, Noh SG, Kim S, Chung HY, Lee H, Moon JO. *Antioxidants*, 2023, 12: 1588
67 Martínez-Reyes I, Chandel NS. *Nat Commun*, 2020, 11: 102
68 Wang Q, Li T, Yang J, Zhao Z, Tan K, Tang S, Wan M, Mao C. *Adv Mater*, 2022, 34: 2201406
69 Wang XB, Jin HF, Tang CS, Du JB. *Eur J Pharmacol*, 2011, 670: 1–6
70 Zhang T, Miao C. *Acta Pharm Sin B*, 2023, 13: 1028–1035
71 Liu X, Khouri-Farah N, Wu CH, Wu GY. *J Gastro Hepatol*, 2020, 35: 2241–2247
72 Meng Z, Geng H, Bai J, Yan G. *Inhalation Toxicol*, 2008, 15: 951–959
73 Li S, Liu R, Jiang X, Qiu Y, Song X, Huang G, Fu N, Lin L, Song J, Chen X, Yang H. *ACS Nano*, 2019, 13: acsnano.8b08700
74 Cowan DB, Yao R, Akurathi V, Snay ER, Thedsanamoorthy JK, Zurakowski D, Ericsson M, Friehs I, Wu Y, Levitsky S, del Nido PJ, Packard AB, McCully JD, Bishopric NH. *PLoS ONE*, 2016, 11: e0160889
75 Ikeda G, Santoso MR, Tada Y, Li AM, Vaskova E, Jung JH, O'Brien C, Egan E, Ye J, Yang PC. *J Am Coll Cardiol*, 2021, 77: 1073–1088
76 Zhou J, Shi Y. *Cell Mol Immunol*, 2023, 20: 555–557
77 Bamshad C, Habibi Roudkenar M, Abedinzade M, Yousefzadeh Chabok S, Pourmohammadi-Bejarpasi Z, Najafi-Ghalehlou N, Sato T, Tomita K, Jahanian-Najafabadi A, Feizkhah A, Mohammadi Roushandeh A. *Int Immunopharmacol*, 2023, 118: 110106